frontiers

Clinopyroxene dissolution records rapid magma ascent

David A. Neave [1,*] **and John Maclennan** [2]

[1] *Department of Earth and Environmental Sciences, The University of Manchester, Manchester, UK*
[2] *Department of Earth Sciences, University of Cambridge, Cambridge, UK*

Correspondence*:
Department of Earth and Environmental Sciences, The University of Manchester,
Williamson Building, Oxford Road, Manchester, M13 9PL, UK
david.neave@manchester.ac.uk

ABSTRACT

Magma ascent rates control volcanic eruption styles. However, the rates at which basaltic magmas ascend through the crust remain highly uncertain. Although recent studies have successfully exploited records of decompression driven degassing to estimate the rates at which H_2O-rich basalts ascend, such approaches cannot readily be applied to primitive and H_2O-poor basalts that erupt in ocean island and mid-ocean ridge settings. Here we present magma ascent rates obtained by modelling the dissolution of clinopyroxene crystals in a wehrlitic nodule from the primitive Borgarhraun lava flow in North Iceland. High-Al_2O_3 clinopyroxene core compositions are consistent with crystallisation near the Moho ($\sim$800 MPa), whereas low-Al_2O_3 clinopyroxene rims and inclusion compositions are consistent with crystallisation at or near the surface. We interpret low-Al_2O_3 rims and inclusions as the crystallised remnants of boundary layers formed by the dissolution of high-Al_2O_3 clinopyroxene during magma ascent. By combining characteristic rim dissolution lengths of 50–100 μm with published experimental calibrations of clinopyroxene dissolution behaviour, we estimate that the Borgarhraun magma most likely decompressed and ascended at rates of 3.0–15 kPa.s^{-1} and 0.11–0.53 m.s^{-1} respectively. These rates are slightly faster than published estimates obtained by modelling the diffusive re-equilibration of olivine crystals, suggesting that the Borgarhraun magma either accelerated upwards or that it stalled briefly at depth prior to final ascent. Comparisons with other basaltic eruptions indicate that the H_2O-poor magma that fed the dominantly effusive Borgarhraun eruption ascended at a similar rate to some H_2O-rich magmas that have fed explosive eruptions in arc settings. Thus, magma ascent rates do not appear to correlate simply with magma H_2O contents. Overall, our findings confirm that primitive and H_2O-poor basalts can traverse the crust within days, and may erupt with little precursory warning of magma ascent.

Keywords: magma ascent rate, plumbing system, clinopyroxene dissolution, basalt, disequilibrium, Iceland

1 INTRODUCTION

Volcanoes are underlain by vertically extensive and geometrically complex magmatic plumbing systems that are capable of dynamically reorganising themselves over the timescales of individual eruptions (Marsh, 2004; Cashman et al., 2017; Sparks and Cashman, 2017; Magee et al., 2018; Maclennan, 2019; Sparks

et al., 2019). It is therefore essential to quantify magma storage and transport timescales if we are to develop accurate models of volcanic behaviour. Magma ascent rates are of particular importance in this respect because they play a central role in determining the style of volcanic eruptions, with eruptions fed by rapidly ascending magmas typically being more explosive than those fed by slowly ascending magmas (Gonnermann and Manga, 2007; Rutherford, 2008). Changes in magma ascent rate can also drive potentially hazardous transitions in eruption style (Woods and Koyaguchi, 1994). Importantly, global systematics in the eruptive behaviour of volcanoes can now be resolved through the local complexity of individual events (Cassidy et al., 2018). However, most published estimates of magma ascent rate are from silicic systems despite the fact that basaltic systems are geographically widespread and dominate global magma budgets (Cassidy et al., 2018, and references therin). Although a number of studies have gone some way towards redressing this imbalance (e.g., Ruprecht and Plank, 2013; Lloyd et al., 2014; Peslier et al., 2015; Newcombe et al., 2020), estimates of magma ascent rate from basaltic systems remain few in number and somewhat uncertain in nature.

Magma ascent rates are commonly estimated using numerical modelling approaches of varying complexity (Wilson and Head, 1981; Mastin, 2002; La Spina et al., 2015, 2019). Analogue modelling approaches have also been used to constrain magma ascent rates and inform the application of numerical models to natural systems (Namiki and Manga, 2006, 2008; Wright et al., 2012). However, ascent rates determined using modelling approaches are often subject to large uncertainties because conduit dimensions and eruptive mass fluxes are often very poorly constrained. Direct estimates of magma ascent rate have been obtained by modelling the diffusive re-equilibration of crystals entrained shortly before eruption (e.g., Ruprecht and Plank, 2013; Mollo et al., 2015; Mutch et al., 2019b; Newcombe et al., 2020), and the diffusive loss of volatiles from melt inclusions and melt embayments as a result of decompression-driven degassing (e.g., Humphreys et al., 2008; Lloyd et al., 2014; Hartley et al., 2018; Barth et al., 2019). Crystal textures have also been used to determine ascent rates in cases where crystallisation kinetics are sufficiently well understood (Armienti et al., 2013). However, ascent rates estimated from the re-equilibration of crystals, whether chemical or textural, convolve isobaric intervals of crystal entrainment with polybaric intervals of magma ascent, and are thus likely to underestimate true values. Although techniques that exploit decompression-driven volatile exsolution circumvent this particular problem, they can only be applied to magmas that degas significantly en route to the surface. Given that primitive basalts from ocean island and mid-ocean ridge settings often degas little during ascent because of their low volatile (i.e. H_2O) contents ($<$0.2 wt.% H_2O; Michael, 1988; Saal et al., 2002; Miller et al., 2019), the rates at which they ascend must be derived using different and volatile-independent approaches.

Basalts frequently carry crystals and nodules formed at depth to the surface, and exploiting the pressure-dependent stability of these crystalline cargoes provides a means of directly estimating the rates at which H_2O-poor primitive basalts ascend (e.g., Brearley and Scarfe, 1986). Clinopyroxene is especially important in this regard because it commonly crystallises from primitive basalts and its stability correlates strongly with pressure (Figure 1; Presnall et al., 1978; Bender et al., 1978; Fujii and Bougault, 1983; Chen and Zhang, 2009; Holland et al., 2018). Clinopyroxene crystals formed at depth may therefore dissolve during ascent, as evidenced by the resorbed nature of phenocrystic and xenocrystic clinopyroxenes erupted from some basaltic volcanoes (e.g., Tsuchiyama, 1986; Gurenko and Sobolev, 2006; Eason and Sinton, 2009). Indeed, the dissolution of clinopyroxene crystals during magma ascent may be responsible for the pyroxene paradox whereby many mid-ocean ridge basalts preserve geochemical signals of clinopyroxene crystallisation but contain no clinopyroxene crystals (O'Donnell and Presnall, 1980; Thompson et al., 1980; Grove et al., 1992).

Here we exploit a quantitative but underused description of clinopyroxene stability in basaltic magmas to estimate the rates at which primitive Icelandic basalts ascend through the crust. We do this by modelling the dissolution of clinopyroxene crystals in a wehrlitic nodule from the Borgarhraun lava flow in North Iceland. Our findings suggest that H_2O-poor basalts from ocean island and mid-ocean ridge systems can ascend as fast as many of their H_2O-rich counterparts from arc systems. This has important implications for evaluating risks posed by basaltic volcanoes as primitive magmas appear capable of traversing the whole crust within a few days.

2 NODULES IN ICELANDIC BASALTS

Basaltic magmas often carry nodules of crystalline material to the surface. These nodules provide crucial insights into the chemical structure of Earth's interior and the dynamics of magmatic plumbing systems (e.g., Rudnick, 1992; Pearson et al., 2003; Holness et al., 2007; Cooper et al., 2016). Magmatic nodules occur in the products of numerous Icelandic eruptions and are variably wehrlitic, gabbroic, troctolitic and feldspathic in composition (Trønnes, 1990; Hansen and Grönvold, 2000; Maclennan et al., 2003a; Gurenko and Sobolev, 2006; Holness et al., 2007). Gabbroic, troctolitic and feldspathic nodules in lavas and tephras from the Eastern Rift Zone of Iceland are thought to constitute the disaggregated remnants of plagioclase-rich crystal mushes from the mid-crust (Hansen and Grönvold, 2000; Holness et al., 2007); macrocrysts and glomerocrysts of anorthitic plagioclase from the same samples are likewise considered to reflect more efficiently disaggregated portions of the same mushes (Halldórsson et al., 2008; Neave et al., 2014). In contrast, wehrlitic, gabbroic and troctolitic nodules from the Miðfell and Borgarhraun lava flows in the Western and Northern Volcanic Zones of Iceland, respectively, are thought to reflect the crystallisation, mixing and reaction of primitive magmas in the lower crust and uppermost mantle (Trønnes, 1990; Maclennan et al., 2003a; Gurenko and Sobolev, 2006). Nodules from the Borgarhraun lava flow are of particular interest because of their extremely primitive compositions [olivine X_{Fo} up to 0.92, where X_{Fo} = molar Mg/(Mg+Fe); plagioclase X_{An} up to 0.92, where X_{An} = molar Ca/(Ca+Na); and clinopyroxene $\mathrm{Mg\#_{cpx}}$ up to 0.90, where $\mathrm{Mg\#_{cpx}}$ = Mg/(Mg+Fe)]. These crystals therefore preserve information about the earliest evolution of mantle-derived melts that would have otherwise been obscured by mixing and sampling bias (Maclennan, 2008; Winpenny and Maclennan, 2011; Neave et al., 2019b).

Nodules from the Borgarhraun lava flow are well suited for estimating primitive basalt ascent rates because there are excellent geobarometric constraints on the pressure (i.e. depth) at which they were stored prior to eruption (Figure 1); the depth from which magma ascended is well known. Clinopyroxene-liquid geobarometry using the model of Putirka et al. (1996) indicates that the Borgarhraun magma was stored at $810\pm110(1\sigma)$ MPa in the uppermost mantle prior to eruption (Winpenny and Maclennan, 2011). The model uncertainty (standard error of estimate, SEE) associated with the geobarometer of Putirka et al. (1996) is 140 MPa. This pre-eruptive storage pressure is corroborated by experimental petrology and geobarometry exploiting the pressure dependence of olivine-plagioclase-augite-melt cotectic positions (Yang et al., 1996; Maclennan et al., 2003b, 2012). In contrast, clinopyroxene-liquid geobarometry using the model of Neave and Putirka (2017) suggests that the Borgarhraun magma was stored within the lower crust at a slightly lower pressure of $570\pm120(1\sigma)$ MPa. This model is also associated with an SEE of 140 MPa. Despite this discrepancy in storage pressure estimates, which probably reflects the model of Neave and Putirka (2017) being optimised for lower pressures and more evolved compositions than those considered here, it is nevertheless clear that the Borgarhraun magma was stored near, and quite probably below, the Moho immediately before eruption.

A further advantage of investigating the Borgarhraun lava flow is that two recent studies into magma storage and ascent timescales provide an excellent framework within which we can interpret our new observations (Mutch et al., 2019a,b). Specifically, Mutch et al. (2019a) exploited the diffusive re-equilibration of spinel chadacrysts within clinopyroxene oikocrysts from wehrlitic nodules to estimate deep magma residence times on the order of 1000 years. Exploiting the diffusive re-equilibration of olivine macrocrysts in the rims of wehrlitic nodules then allowed Mutch et al. (2019b) to estimate transcrustal magma transport times on the order of 10 days that correspond to minimum magma ascent rates of 0.02–0.1 $m.s^{-1}$.

Here we investigate a wehrlitic nodule in sample JM27 collected in July 1999 from the eastern edge of the Borgarhraun lava flow (65°51.05'N, 16°59.93'W). Although nodules with variably dunitic, wehrlitic, gabbroic and troctolitic compositions have been described from the same location by Maclennan et al. (2003a), we focus on wehrlitic sample JM27 for three reasons: firstly, the abundance of clinopyroxene makes it possible to robustly constrain the minimum apparent dissolution lengths required to avoid dissolution time estimates being compromised by 3-D cutting effects; secondly, the presence of variably orientated crystals allows the effects of anisotropy on apparent dissolution lengths to be evaluated; and thirdly, the nodule's internal porosity likely prevented the dissipation dissolution textures by convection or turbulent mingling. Nevertheless, we note that other nodules described by Maclennan et al. (2003a) also show similar features to those we describe in sample JM27 (Supplementary Material), indicating that our findings are applicable to the Borgarhraun eruption as a whole.

3 METHODS

QEMSCAN imaging of sample JM27 was performed on a FEI Quanta-650F instrument in the Department of Earth Sciences at the University of Cambridge, UK. Images were collected with a 4-μm pixel spacing, and 2000-count EDX spectra were used to produce phase and Al concentration maps following the principles discussed by Pirrie et al. (2004) and Neave et al. (2017a). Additional backscattered electron (BSE) imaging was performed on a Phillips FEI XL30 instrument in the Department of Earth and Environmental Sciences at the University of Manchester, UK.

Mineral compositions were determined by electron probe microanalysis (EPMA) on a Cameca SX100 instrument in the Department of Earth Sciences at the University of Cambridge, UK. Silicon, Ti, Al, Cr, Fe, Mn, Mg, Ca, Na, K and Ni were measured in minerals with an accelerating voltage of 15 kV. Olivine, clinopyroxene and spinel were measured with a current of 20 nA and a spot size of 1 μm. Plagioclase was measured with a current of 10 nA and a spot size of 5 μm. The following standards were used for calibration: diopside (Si and Ca), rutile (Ti), corundum (Al), Cr metal (Cr), fayalite (Fe), Mn metal (Mn), St. Johns olivine (Mg), jadeite (Na), orthoclase (K) and NiO (Ni). Peak and background counting times were typically 20 and 10 s respectively for major elements and 40 and 20 s respectively for minor elements, with the exception of Na that was counted on-peak for 10 s. Data quality was monitored by measuring the following secondary standards (representative analyses are provided in the Supplementary Material): San Carlos olivine (NMNH 111312–44), Lake County plagioclase (NMNH 115900), Kakanui augite (NMNH 122142) and Ney County Cr-augite (NMNH 164905) (Jarosewich et al., 1980, 1987). Accuracy and precision are both estimated as $\leq$1% relative for major elements (present at $>$1 wt.%) and $\leq$5% relative for minor elements (present at $<$1 wt.%).

4 RESULTS

4.1 Petrography and QEMSCAN imaging

The wehrlitic nodule in sample JM27 is composed of clinopyroxene with subordinate olivine and rare plagioclase (Figures 2a and 3a; Supplementary Material). Equant clinopyroxene crystals in the nodule are typically 500 μm to 1 mm in diameter, while equant olivine crystals are typically 200–500 μm in diameter. Rare tabular plagioclase crystals up to 250 μm in length also occur. The nodule hosts a network of microcrystalline pockets and embayments of groundmass that are contiguous with the host lava groundmass (Figure 3b). These pockets and channels are sometimes vesiculated, indicating that the nodule was porous to its host lava prior to lava flow emplacement. Both lava and nodule groundmasses are composed of high-aspect-ratio plagioclase crystals intergrown with small crystals of olivine, clinopyroxene and ilmenite (Figure 3b). The boundary between the wehrlitic nodule and the groundmass – defined by the limit of connected clinopyroxene crystals – is highly sinuous (Figure 2a). Crystals of olivine, plagioclase and clinopyroxene occur outside the nodule both as individual macrocrysts and as macrocrysts within monomineralic and polymineralic glomerocrysts (Figures 2a and 3d). Typical macrocrystic and glomerocrystic crystal diameters span the following ranges: 200 μm to 2 mm for olivine; 200–800 μm for plagioclase; and 200–800 μm for clinopyroxene. Glomerocrystic plagioclase and clinopyroxene crystals often occur in ophitic arrangements (Figure 3d).

QEMSCAN phase maps highlight abundant plagioclase inclusions within the cores of nodule clinopyroxene crystals that have not been described in previous studies (Figure 2b). These plagioclase inclusions are typically 20–100 μm in length and irregular to vermicular in form (Figure 3a). Many plagioclase inclusions are associated with small (10–50 μm) and irregular pockets of mesostasis that are texturally distinct from spheroidal melt inclusions (Figure 3c). Numerous small crystals of plagioclase also occur within the rims of nodule clinopyroxene crystals. Some of these crystals are separated from the groundmass by their host crystals and represent true inclusions. Others form continuous chains of crystals that extend from clinopyroxene rims deep into the interior of clinopyroxene cores. Within the limited compositional resolution of QEMSCAN phase identification, plagioclase inclusions have similar compositions to groundmass plagioclase crystals (bytownitic to labradoritic), while plagioclase macrocrysts and nodule plagioclase crystals are more primitive (anorthitic to bytownitic).

Semi-quantitative Al concentration maps indicate that plagioclase inclusions are located within domains of low-Al_2O_3 clinopyroxene that also appear to form inclusions within high-Al_2O_3 clinopyroxene cores (Figure 2c). Note that we refer to these low-Al_2O_3 clinopyroxene domains as inclusions without implying any genetic connotations. In other words, low-Al_2O_3 clinopyroxene inclusions are simply considered as domains of low-Al_2O_3 clinopyroxene that appear to be enclosed by high-Al_2O_3 clinopyroxene. Importantly, the presence and nature of these low-Al_2O_3 clinopyroxene inclusions was only revealed through Al concentration mapping; variations in clinopyroxene Al_2O_3 content were not apparent during optical microscopy or phase mapping. Nodule clinopyroxene rims have similarly low Al_2O_3 contents to clinopyroxene inclusions. Indeed, the chains of plagioclase crystals described in the preceding paragraph lie within low-Al_2O_3 channels that extend from clinopyroxene rims deep into their cores. Low-Al_2O_3 clinopyroxene inclusions are on the order of 50–250 μm in diameter, while the thinnest nodule clinopyroxene rims – those least affected by sectioning effects – are 50–100 μm wide.

High-Al_2O_3 clinopyroxene cores have relatively low BSE intensities while low-Al_2O_3 clinopyroxene rims and inclusions have relatively high BSE intensities (Figures 3a and 3b). Boundaries between nodule clinopyroxene cores and rims are often rounded (Figure 3b). As previously documented by Winpenny

and Maclennan (2011), subtle variations in BSE intensity within nodule clinopyroxene cores delimit sector zones. Patchy variations in BSE intensity also occur at the edges of some clinopyroxene inclusions (Figure 3a), but appear to represent complex interfaces between inclusions and their host crystals rather than zoning intrinsic to low-Al_2O_3 clinopyroxene inclusions (Figures 3b and 3c). Importantly, we see no crystallographically controlled variations in BSE intensity that would reveal the presence of exsolution lamellae within nodule clinopyroxene cores (e.g., Holness et al., 2011).

Although BSE intensity is broadly constant within low-Al_2O_3 clinopyroxene inclusions, some inclusions contain films and pockets of very high BSE intensity (Figure 3c). These films and pockets typically occur next to plagioclase inclusions and along the inclusions' boundaries with high-Al_2O_3 clinopyroxene hosts, suggesting that they represent domains of late-stage crystallisation. Further evidence for late-stage crystallisation is provided by the small oxide crystals (5–20 μm in diameter, and subsequently identified as titanomagnetite) that occur along some interfaces between plagioclase inclusions and portions of clinopyroxene inclusions with very high BSE intensities (Figure 3c).

4.2 Electron probe microanalysis

Plagioclase and olivine compositions from sample JM27 are summarised in Figure 4. Plagioclase compositions range from X_{An} = 0.70 to X_{An} = 0.91 (Figure 4a), and different compositions are found in different textural associations. High X_{An} contents (>0.85) are only found in rare nodule plagioclase cores and the cores of some macrocrysts and glomerocrysts. Moderate X_{An} contents (0.78–0.85) are found in nodule plagioclase rims, some plagioclase inclusions and in the cores and rims of some macrocrysts and glomerocrysts. Low X_{An} contents (<0.78) are found in some plagioclase inclusions and the outermost rims of macrocrysts, glomerocrysts and nodule plagioclase crystals. These low X_{An} contents are typically located close to films and pockets of late-stage crystallisation (Figure 3c). Olivine compositions range from X_{Fo} = 0.81 to X_{Fo} = 0.90 (Figure 4b). Relationships between composition and texture are less clear for olivine than plagioclase, though nodule, macrocryst and glomerocryst olivine cores typically contain the highest X_{Fo} contents (>0.85). Lower X_{Fo} contents (0.82–0.85) are found in the cores and rims of some macrocrysts and glomerocrysts, and the lowest X_{Fo} content measured (0.81) is from a nodule olivine rim in contact with the groundmass.

Clinopyroxene compositions are summarised in Figures 5 and 6, and range from $Mg\#_{cpx}$ = 0.35 to $Mg\#_{cpx}$ = 0.91, with the majority of compositions lying between $Mg\#_{cpx}$ = 0.85 and $Mg\#_{cpx}$ = 0.90. Different clinopyroxene compositions are closely linked with different textural associations. Nodule clinopyroxene cores are primitive ($Mg\#_{cpx}$ = 0.88–0.91; Figures 5 and 6) and rich in octahedral Al (Al_{vi} = 0.08–0.11, where Al_{vi} is calculated on a six-oxygen basis; Figure 6a). They are also somewhat enriched in jadeite component [X_{Jd} = 0.012–0.018, where X_{Jd} is calculated following Putirka (2008); Figure 6b]. Variability in TiO_2 (0.11–0.20 wt.%; Figure 5b), Al_2O_3 (4.0–5.5 wt.%; Figure 5d) and wollastonite component [X_{Wo} = 0.41–0.44, where X_{Wo} = Ca/(Ca+Mg+Fe) on a molar basis; Figure 5f] over the range of $Mg\#_{cpx}$ contents present in nodule clinopyroxene cores reflects sector zoning (Figure 3a). Some macrocryst and glomerocryst cores have similar compositions to nodule clinopyroxene cores (i.e. $Mg\#_{cpx}$ = 0.88–0.90 and Al_{vi} = 0.09–0.11), while others are slightly more evolved. Nodule clinopyroxene rims are consistently more evolved than nodule clinopyroxene cores ($Mg\#_{cpx}$ = 0.72–0.88), a feature highlighted by the positive correlation between $Mg\#_{cpx}$ and TiO_2 defined by analyses from nodule clinopyroxene rims (Figure 5b). Rims are also considerably poorer in Al_{vi} (<0.08; Figure 6a) and slightly poorer in X_{Jd} (<0.014; Figure 6b) that nodule clinopyroxene cores. Some macrocryst and glomerocryst compositions overlap with nodule clinopyroxene compositions, though a few of analyses extend to much more evolved compositions ($Mg\#_{cpx}$

reaches as low as 0.55 and TiO_2 reaches as high as 1.0 wt.%), probably reflecting late-stage crystallisation during lava flow emplacement.

Clinopyroxene inclusions are the most compositionally variable of all clinopyroxene textural types ($Mg\#_{cpx}$ = 0.35–0.90). The majority of inclusion analyses fall within a compositional range shared with some macrocryst and glomerocryst analyses, as well as with analyses from nodule clinopyroxene rims ($Mg\#_{cpx}$ = 0.85–0.87, Al_2O_3 = 2.0–3.0 wt.% and Al_{vi} = 0.03–0.06; Figures 5b, 5d and 6a). These analyses are located within constant-BSE-intensity domains of clinopyroxene inclusions (Figure 3a). A primitive subpopulation of analyses from patchy zones at inclusion edges overlaps with analyses from nodule clinopyroxene core compositions ($Mg\#_{cpx}$ = 0.88–0.90, Al_2O_3 = 4.5–5.0 wt.% and Al_{vi} = 0.08–0.09), and probably constitutes analyses of complex, folded interfaces between inclusions and nodule clinopyroxene cores (Figure 3b). An evolved subpopulation of inclusion analyses overlaps partly with analyses from nodule clinopyroxene rims. These analyses are located within domains of very high BSE intensity that we have interpreted as pockets of late-stage crystallisation (Figure 3c). The inflection of TiO_2 content with decreasing $Mg\#_{cpx}$ within this subpopulation reflects the onset of titanomagnetite crystallisation.

5 IDENTIFYING CLINOPYROXENE DISSOLUTION

High-Mg# clinopyroxene crystals in the Borgarhraun lava flow record high pre-eruptive magma storage pressures of 570–810 MPa (Winpenny and Maclennan, 2011; Neave and Putirka, 2017). These pressures are consistent with the high Al_2O_3, Al_{vi} and X_{Jd} contents of macrocryst, glomerocryst and nodule clinopyroxene cores investigated here, confirming the ultimately deep origin of sample JM27 (Figures 3, 5b, 5c and 6; Aoki and Kushiro, 1968; Thompson, 1974; Blundy et al., 1995; Putirka et al., 1996). Given that the liquidus temperature of clinopyroxene is significantly higher at 570–810 MPa than 1 atm in Borgarhraun-like magmas [90–140 °C higher according to calculations with the MELTS algorithm (Figure 1; Ghiorso and Sack, 1995; Smith and Asimow, 2005), and 70–120 °C higher according to calculations on a compositionally analogous basalt from the Reykjanes Peninsula with THERMOCALC (RE46; Yang et al., 1996; Holland et al., 2018)], clinopyroxene crystals formed near the Moho are thus unlikely to have been in equilibrium with their carrier liquids upon eruption. Assuming that the ascending Borgarhraun magma cooled along an adiabatic gradient of <1 °C.km^{-1} (Katz et al., 2003), it seems probable that deep-formed high-Al_2O_3 clinopyroxene crystals would have at least partly dissolved en route to the surface.

The rounded nature of high-Al_2O_3, high-Al_{vi} and high-X_{Jd} nodule clinopyroxene cores indicates that they underwent dissolution prior to their encapsulation within low-Al_2O_3, low-Al_{vi} and low-X_{Jd} rims at or near the surface (Figures 3b, 5b, 5c and 6; Aoki and Kushiro, 1968; Thompson, 1974; Blundy et al., 1995; Putirka et al., 1996). A low-pressure origin for clinopyroxene rims is indicated by comparisons with the products of 1-atm experiments performed by Yang et al. (1996), as well as by clinopyroxene-liquid geobarometry performed on nodule clinopyroxene rims using the model of Neave and Putirka (2017). Geobarometry was undertaken on clinopyroxene rims using the matrix glass composition of Sigurdsson et al. (2000), and returned a pressure of $210\pm35(1\sigma)$ MPa with an associated model SEE of 140 MPa. All clinopyroxene-liquid pairs were checked for multicomponent equilibrium following the approach of Neave et al. (2019a). Although 210 MPa is appreciably greater than 1 atm, it is, model uncertainties notwithstanding, considerably lower than the 570–810 MPa range obtained from high-Al_2O_3 cores (Figure 1; Winpenny and Maclennan, 2011; Neave and Putirka, 2017). Moreover, that only a few analyses passed equilibrium filters (n = 3) suggests that clinopyroxene rims crystallised under disequilibrium conditions, feasibly resulting in the overestimation of crystallisation pressures (Mollo et al., 2010).

The presence of abundant low-Al_2O_3 clinopyroxene inclusions within high-Al_2O_3 nodule clinopyroxene cores implies that dissolution was not only restricted to crystal faces, but also permeated crystal cores (Figure 3a). Similar textures have been described in clinopyroxene macrocrysts from Haleakala volcano in Hawaii by Welsch et al. (2016), but were attributed to rapid, kinetically controlled crystal growth rather than dissolution. These authors came to this interpretation because both low-Al_2O_3 and high-Al_2O_3 domains of clinopyroxene macrocrysts are in contact the groundmass in their samples, indicating that they grew concurrently. However, only low-Al_2O_3 rims are in contact the groundmass in sample JM27, ruling out concurrent growth in our case. Low-Al_2O_3 clinopyroxene inclusions in the Borgarhraun lava flow also cut across boundaries between sector zones within high-Al_2O_3 nodule clinopyroxene cores, demonstrating that the inclusions formed by the resorption of pre-existing crystal cores. The occurrence of low-Al_2O_3 clinopyroxene embayments within high-Al_2O_3 cores also suggests that clinopyroxene inclusions may represent ramifying networks of low-Al_2O_3 clinopyroxene channels in 3-D rather than isolated inclusions of the kind visible in 2-D. Indeed, the compositional similarity between clinopyroxene inclusions and nodule clinopyroxene rims suggests that they share a common dissolution-reprecipitation origin that we discuss in detail below (Figure 5). Finally, domains of patchy zoning associated with complex interface geometries between inclusions and their host crystals are similar to cellular dissolution textures in other systems (Figure 3b; Streck, 2008), highlighting dissolution's central role in clinopyroxene inclusion genesis.

Importantly, our observations from the Borgarhraun lava flow are not unique; similar observations from lavas erupted elsewhere in Iceland validate our identification of substantial clinopyroxene dissolution. For example, Trønnes (1990) and Hansteen (1991) described resorbed 'Al- and Cr-rich endiopside' crystals equivalent to our nodule clinopyroxene cores in primitive basalts from the Hengill volcanic system in the Western Rift Zone. Gurenko and Sobolev (2006) also describe spongy and embayed high-Al_2O_3 clinopyroxene crystals in glass-hosted nodules from the primitive Miðfell lava flow, also from the Hengill volcanic system, though these authors account for dissolution by melt-rock reaction rather than decompression during ascent. Clinopyroxene dissolution has also been proposed as an explanation for the chemical systematics of lavas from both the Eastern and Western Rift Zones (Halldórsson et al., 2008; Eason and Sinton, 2009), illustrating its potentially widespread role in basalt petrogenesis.

In contrast with the glassy nodules from the Miðfell lava flow described by Gurenko and Sobolev (2006), the wehrlitic nodule we describe here is fully crystalline; gabbroic and troctolitic nodules collected from the same location are similarly crystalline (Supplementary Material). Thus, while previously studied clinopyroxenes from the Miðfell lava flow are surrounded by glass, those we have studied from the Borgarhraun lava flow are surrounded by low-Al_2O_3 clinopyroxene rims. They are also permeated by low-Al_2O_3 clinopyroxene inclusions that host inclusions of relatively low-X_{An} plagioclase. This important textural difference – the presence or absence of low-Al_2O_3 clinopyroxene around and within high-Al_2O_3 clinopyroxene cores – reflects the contrasting emplacement histories of the Miðfell and Borgarhraun lava flows. Specifically, the Miðfell lava flow was erupted subglacially, making it possible for Gurenko and Sobolev (2006) to collect glassy material from rapidly quenched pillow basalt rims. In contrast, the Borgarhraun lava flow erupted subaerially, meaning that sample JM27 cooled slowly and crystallised in situ. The relatively slow cooling of the Borgarhraun lava flow did however allow important information about the extent of pre-eruptive high-Al_2O_3 dissolution to be captured. Namely, low-Al_2O_3 clinopyroxene rims and inclusions record the approximate dimensions of boundary layers formed by the dissolution of high-Al_2O_3 clinopyroxene during magma ascent which are then preserved during cooling by the high closure temperature of major element diffusion within clinopyroxene (Freer et al., 1982).

Fractional crystallisation calculations performed on the mean composition of high-Al_2O_3 nodule clinopyroxene cores with the MELTS algorithm at 1 atm reproduce the phase assemblage and phase proportions observed in clinopyroxene rims and inclusions (Ghiorso and Sack, 1995; Smith and Asimow, 2005). Crystallisation was assumed to be fractional because lava flow cooling rates probably outpaced mineral-mineral equilibration rates. Olivine crystallisation was also suppressed in favour of epitactic clinopyroxene growth. Calculations were performed without imposing oxygen fugacity constraints; oxygen fugacity was imposed from the starting clinopyroxene Fe^{2+}/Fe^{3+} estimated by charge balance following Lindsley and Andersen (1983). Once the calculated mass fraction of melt (F) reached 0.05, calculated mass fractions of clinopyroxene, plagioclase and spinel-structured oxide were 0.89, 0.05 and 0.01 respectively, broadly in line with BSE observations from clinopyroxene inclusions (Figures 3a and 3c). Melts with the mean composition of high-Al_2O_3 nodule clinopyroxene cores thus crystallise clinopyroxene and plagioclase in a ratio of $\sim$18:1, a ratio much closer to that observed in clinopyroxene inclusions than the $\sim$1:1 ratio calculated to result from matrix glass crystallisation at 1 atm (Figures 3a and 3b). Moreover, pigeonite was predicted to crystallise at $F < 0.12$, consistent with the low X_{Wo} content of low-$Mg\#_{\mathrm{cpx}}$ analyses from rims and inclusions associated with pockets of late-stage crystallisation (Figures 3c and 5e).

Despite calculations with the MELTS algorithm reproducing the phase assemblage and phase proportions observed in clinopyroxene inclusions, they nevertheless return consistently higher $Mg\#_{\mathrm{cpx}}$ and X_{An} than observed in sample JM27 ($Mg\#_{\mathrm{cpx}} > 0.9$ until $F < 0.25$ and $X_{\mathrm{An}} > 0.8$ until $F < 0.15$). Although discrepancies between calculations with the MELTS algorithm and observations from both natural and experimental systems are well documented (e.g., Neave et al., 2019b), they are probably exacerbated in this case by differences between the mean composition of high-Al_2O_3 nodule clinopyroxene cores and the compositions for which the MELTS algorithm has been calibrated (Ghiorso and Sack, 1995). However, a more fundamental explanation for these discrepancies stems from assuming that the boundary layers created by clinopyroxene dissolution were closed and compositionally homogeneous systems for their entire lifespans. Although these assumptions make performing illustrative calculations with the MELTS algorithm tractable, they are incorrect in detail. This is because our observations suggest Mg-rich and Na-poor high-Al_2O_3 clinopyroxene cannot be mass balanced against a Mg-poor and Na-rich assemblage containing low-Al_2O_3 clinopyroxene, plagioclase and titanomagnetite.

The dissolution rate of crystals is strongly controlled by the diffusivity of their constituent components in their surrounding melts. This results in the creation of concentration gradients around dissolving crystals (e.g., Zhang et al., 1989). Mean boundary layer compositions will therefore lie between those of dissolving crystals and their host melts. This may account for the slightly lower Mg# of most clinopyroxene inclusion and nodule clinopyroxene rim analyses (i.e. those not associated with pockets of late-stage crystallisation) with respect to nodule clinopyroxene core analyses (Figure 5). Boundary layer compositions will also depend on the relative diffusivities of different elements, meaning that some exchange with the surrounding melt is highly likely to occur; even convectively stable boundary layers are unlikely to be fully isolated from the surrounding melt. Complex multicomponent effects notwithstanding (e.g., Liang et al., 1996), Na typically diffuses more quickly than other major species in silicate melts (Zhang et al., 2010b), providing a mechanism by which initially Na-poor boundary layers could have acquired sufficient Na to crystallise $X_{\mathrm{An}} \leq 0.82$ plagioclase. In contrast, Al diffuses more slowly than most other major species in silicate melts (Chen and Zhang, 2008; Yu et al., 2016), providing a mechanism by which Al-poor boundary layers formed by dissolution could have been preserved during magma ascent (cf. Neave et al., 2017b). However, evaluating the exact composition of boundary layers in sample JM27 would be challenging, and we suggest that such information would be best recovered from glassy nodules with feasibly intact boundary layers (e.g., Gurenko and Sobolev, 2006).

The narrowest nodule clinopyroxene rims we observed are typically 50–100 μm wide (Figure 3a and 3b). These minimum rim widths provide our best estimates of the distances that nodule clinopyroxene cores dissolved during ascent. This is because they are probably associated with crystal faces oriented normal to the plane of the thin section that are hence are minimally affected by 3-D cutting effects (e.g., Shea et al., 2015). Moreover, rim widths do not appear to vary substantially between different crystal faces, indicating that mineral anisotropy does not significantly affect clinopyroxene dissolution lengthscales in sample JM27. Clinopyroxene inclusions and embayments probably resulted from dissolution over greater distances than 100 μm, but may also reflect the exploitation of pre-existing fractures and cleavage planes (Chen and Zhang, 2009). It is also possible that the development of dissolution channels in 3-D may have affected the apparent dissolution lengths visible in 2-D. Importantly, the geometry of the wehrlitic nodule investigated here means that nodule clinopyroxene rims were largely protected from turbulence in the external magma during ascent. That is, we expect that nodule clinopyroxene rims record dissolution that was primarily diffusive rather than convective in nature (Kerr, 1995; Zhang and Xu, 2003). As a consequence, the thickness of nodule clinopyroxene rims encodes robust information about clinopyroxene dissolution times that can be used to estimate magma decompression and ascent rates.

6 MODELLING CLINOPYROXENE DISSOLUTION

Experimental investigations of clinopyroxene dissolution by Chen and Zhang (2009) provide a framework for modelling clinopyroxene dissolution recorded in the Borgarhraun lava flow. Specifically, Chen and Zhang (2009) characterised rates of diffusive diopside dissolution into a tholeiitic basalt by experimentally dissolving diopside crystals at a range of pressures and temperatures. They then used their experimental results to calibrate a model from which dissolution time could be predicted as a function of pressure, temperature, melt composition, clinopyroxene composition and dissolution length. We do however note the important limitation that Chen and Zhang (2009) did not incorporate any effects of mineral anisotropy into their simplified model. Nevertheless, coherence in their experimental results suggests that anisotropy exerts only second order effects over crystal dissolution rates. Importantly, dissolution experiments were carefully designed to avoid convection, making the resulting model well suited for estimating dissolution times from the nodule clinopyroxene rims we describe here. Furthermore, the high-$Mg\#_{cpx}$ compositions from the Borgarhraun lava flow are amongst the closest to pure diopside of any known compositions from Iceland (Maclennan et al., 2003a; Winpenny and Maclennan, 2011), making the Borgarhraun eruption an ideal candidate for estimating magma decompression and ascent rates using a model based on diopside dissolution. Moreover, clinopyroxene crystals in JM27 are free from exsolution lamellae that may complicate the interpretation of features created by diffusion and dissolution processes (e.g., Dohmen and Milke, 2010).

Chen and Zhang (2009) provided a series of five equations (their equations 4, 5a, 5b, 5c and 5d) that, in theory, can be solved iteratively to obtain the parameters required to quantitatively relate dissolution length and dissolution time in diopside-liquid systems. However, our attempts to iteratively solve these equations with the optim() function in the stats package of R often failed to converge (R Development Core Team, 2016), making it difficult to explore clinopyroxene stability across diverse pressure and temperature conditions. We therefore rearranged the equations of Chen and Zhang (2009) to reduce the number of unknown parameters from five to one, allowing the single remaining unknown parameter (the fitting parameter α) to be obtained through a more stable root-finding approach implemented with the uniroot() function in the stats package of R. These rearrangements are documented below.

As described by Chen and Zhang (2009) in their equation 2a, chemical profiles in melts adjacent to dissolving crystals can be described by the 1-D diffusive dissolution equation (Crank, 1975):

$$C = C_\infty + (C_0 - C_\infty)\frac{\mathrm{erfc}\left(\frac{x}{2\sqrt{Dt}} - \alpha\right)}{\mathrm{erfc}\,(-\alpha)}, \tag{1}$$

where C is the concentration of a component in the melt, C_0 is concentration in the melt at the crystal-melt interface and C_∞ is the far-field concentration. x is the distance from the crystal-melt interface, D is the effective binary diffusivity of the element or oxide in question and t is duration of experiment. α is a fitting parameter related to the dissolution rate that, as per equation 2b of Chen and Zhang (2009), satisfies:

$$\exp(\alpha^2)\,\mathrm{erfc}\,(-\alpha)\sqrt{\pi}\alpha = \frac{C_0 - C_\infty}{C_c - C_0}, \tag{2}$$

where C_c is the concentration of the element or oxide in question in the crystal.

As per equation 2c of Chen and Zhang (2009), the crystal diffusive dissolution distance can be expressed as:

$$L = 2\alpha\frac{\rho_m}{\rho_c}\sqrt{Dt}, \tag{3}$$

where ρ_m and ρ_c are the densities of melt and crystal respectively.

The stability of clinopyroxene crystals in basaltic melts is mediated, in part, by the diffusion of Mg and Ca cations within their host liquids (Chen and Zhang, 2009); the diffusion of Mg and Ca within clinopyroxene crystals is many orders of magnitude slower than within basaltic melts (Zhang et al., 2010a), and thus does not affect clinopyroxene stability over the timescales of interest here. As per equations 3a and 3b of Chen and Zhang (2009), Mg and Ca diffusion within basaltic melts can be described by:

$$\ln D_{\mathrm{Mg}} = -6.664(\pm 0.745) - \frac{28897 \pm 1221(2\sigma)}{T}, \tag{4}$$

and:

$$\ln D_{\mathrm{Ca}} = -10.517(\pm 0.901) - \frac{21205 \pm 1476(2\sigma)}{T}, \tag{5}$$

where T is in K and D is in $\mathrm{m}^2.\mathrm{s}^{-1}$.

As per equation 4 of Chen and Zhang (2009), the saturation condition at the clinopyroxene-melt interface can be expressed when:

$$\ln\left(C_0^{\mathrm{Mg}} \times C_0^{\mathrm{Ca}}\right) = a + bP + \frac{e}{T} + g\frac{P^2}{T^2}, \tag{6}$$

where C_0 values are expressed in oxide wt.%, P is pressure in GPa and a, b, e and g are fitting parameters with values of $22.85\pm1.82(2\sigma)$, $2.10\pm0.44(2\sigma)$, $26360\pm2565(2\sigma)$ and $1.22\pm0.43(2\sigma) \times 10^6$ respectively.

Rearranging equation 6 and gathering the terms then allows us to define a function in which $C_0^{\mathrm{Mg}} \times C_0^{\mathrm{Ca}}$ depends upon P and T alone:

$$H(P,T) = a + bP + \frac{e}{T} + g\frac{P^2}{T^2}, \tag{7}$$

and thus:

$$C_0^{\mathrm{Mg}} \times C_0^{\mathrm{Ca}} = \exp\left(H(P,T)\right) = h(P,T). \tag{8}$$

Given that L is equal for both MgO and CaO, equation 3 leads to the expression:

$$\alpha_{\mathrm{Mg}} = \alpha_{\mathrm{Ca}}\sqrt{\frac{D_{\mathrm{Ca}}}{D_{\mathrm{Mg}}}}. \tag{9}$$

If we define:

$$f(\alpha) = \exp\left(\alpha^2\right)\operatorname{erfc}\left(-\alpha\right)\sqrt{\pi}\alpha, \tag{10}$$

then rearranging equation 2 provides:

$$f(\alpha) = \frac{C_0 - C_\infty}{C_c - C_0}. \tag{11}$$

Given that, as per equation 8, $C_0^{\mathrm{Mg}} = h/C_0^{\mathrm{Ca}}$, then:

$$f(\alpha_{\mathrm{Mg}}) = \frac{(h/C_0^{\mathrm{Ca}}) - C_\infty^{\mathrm{Mg}}}{C_c^{\mathrm{Mg}} - (h/C_0^{\mathrm{Ca}})}, \tag{12}$$

and:

$$f(\alpha_{\mathrm{Ca}}) = \frac{C_0^{\mathrm{Ca}} - C_\infty^{\mathrm{Ca}}}{C_c^{\mathrm{Ca}} - C_0^{\mathrm{Ca}}}. \tag{13}$$

Rearranging these equations then gives:

$$C_0^{\mathrm{Ca}} = \frac{h[1 + f(\alpha_{\mathrm{mg}})]}{f(\alpha_{\mathrm{Mg}})C_c^{\mathrm{Mg}} + C_\infty^{\mathrm{Mg}}} = \frac{f(\alpha_{\mathrm{Ca}})C_c^{\mathrm{Ca}} + C_\infty^{\mathrm{Ca}}}{1 + f(\alpha_{\mathrm{Ca}})}, \tag{14}$$

and therefore:

$$h[1 + f(\alpha_{\mathrm{Mg}})][1 + f(\alpha_{\mathrm{Ca}})] = [f(\alpha_{\mathrm{Ca}})C_c^{\mathrm{Ca}} + C_\infty^{\mathrm{Ca}}][f(\alpha_{\mathrm{Mg}})C_c^{\mathrm{Mg}} + C_\infty^{\mathrm{Mg}}] \tag{15}$$

A root finding approach can then be used to find values of α_{Mg} where the following expression is zero and substitutions are made using equation 9:

$$Q = h[1 + f(\alpha_{\mathrm{Mg}})][1 + f(\alpha_{\mathrm{Ca}})] - [f(\alpha_{\mathrm{Ca}})C_c^{\mathrm{Ca}} + C_\infty^{\mathrm{Ca}}][f(\alpha_{\mathrm{Mg}})C_c^{\mathrm{Mg}} + C_\infty^{\mathrm{Mg}}], \quad (16)$$

and equation 3 can then be used to calculate t.

The results of dissolution calculations performed assuming a fixed dissolution time of 1 s are presented in Figure 7 and demonstrate the strong effects of pressure and temperature on the stability of clinopyroxene with the mean composition of nodule clinopyroxene cores in the Borgarhraun matrix glass composition reported by Sigurdsson et al. (2000). Calculated clinopyroxene liquidus temperatures vary from ∼1190 °C at 1 atm to ∼1320 °C at 800 MPa and are encouragingly consistent with the results of calculations with the MELTS algorithm (Figure 1). These calculations also illustrate the strong dependence of dissolution rate on temperature and hence the vital importance of estimating magma eruption temperatures accurately when determining magma decompression and ascent rates from clinopyroxene dissolution lengths.

Indicative clinopyroxene dissolution times for the Borgarhraun lava flow were estimated by assuming that all dissolution took place at the surface following instantaneous magma ascent from near-Moho depths (Figure 8). A magma temperature of 1230 °C was taken from Mutch et al. (2019b) who performed calculations with the geothermometer of Sugawara (2000) that has an associated model SEE of 30 °C. The temperature decrease associated with adiabatic cooling of the ascending magma over the pressure interval of relevance is well within the SEE of the geothermometer used (<8 °C over 215 MPa; see below; Katz et al., 2003), and is thus not considered further. Uncertainties in dissolution time estimates were evaluated by resampling (n = 1000) temperature and fitting parameters in equation 6 for each dissolution length increment according to their respective uncertainties (Sugawara, 2000; Chen and Zhang, 2009). Resulting median dissolution times range from 30 min for a dissolution length of 50 μm to 150 min for a dissolution length of 100 μm – the range of minimum observed dissolution lengths (Figure 3). Lower 1σ bounds on dissolution times (i.e. 17$^{\mathrm{th}}$ percentiles) are typically a factor of ten shorter than the median times and 1σ bounds (83$^{\mathrm{rd}}$ percentiles) are typically a factor of 18 longer. Dissolution times are thus associated with 1σ uncertainties on the order of one order of magnitude that primarily reflect uncertainties in magma eruption temperatures which are challenging to overcome with currently available approaches (Putirka, 2008).

Mean magma decompression rates were estimated from clinopyroxene dissolution times by assuming that dissolution started as soon the ascending magma reached a pressure of 215 MPa, the pressure at which equations 3 and 6 predict a change from clinopyroxene crystallisation to clinopyroxene dissolution (Figure 7). Estimated mean decompression rates vary from 110 kPa.s^{-1} for a dissolution length of 50 μm to 24 kPa.s^{-1} for a dissolution length of 100 μm (Figure 9a). Estimated rates increase substantially to 210 MPa.s^{-1} for a dissolution length of 5 μm, and decrease modestly to 3.3 kPa.s^{-1} for a dissolution length of 300 μm. Mean magma ascent rates were estimated by converting the clinopyroxene saturation pressure of 215 MPa into a depth of 7.6 km by assuming a mean crustal density of 2.88 Mg.m^{-3} (Maclennan et al., 2001). Resulting mean ascent rate estimates vary from 3.9 m.s^{-1} for a dissolution length of 50 μm to 0.85 m.s^{-1} for a dissolution length of 100 μm (Figure 9b), and are subject to propagated uncertainties on order of one order of magnitude. However, assuming that all dissolution occurred at the surface following instantaneous ascent is likely to overestimate true magma decompression and ascent rates because it unrealistically implies that all dissolution occurred under the high degrees of disequilibrium. In line with other studies (e.g., Lloyd et al., 2014; Mutch et al., 2019b; Newcombe et al., 2020), we therefore performed additional calculations with the more naturalistic assumption that magma ascended at a constant rate.

Assuming that clinopyroxene dissolution took place in response to decompression at a constant rate, dissolution lengths of 50 and 100 μm imply decompression rates of 15 and 3.0 kPa.s^{-1} respectively (Figure

9a). These values are approximately one order of magnitude lower than the mean decompression rates estimated by assuming that all dissolution took place following instantaneous ascent. Estimated magma ascent rates are also correspondingly lower: 0.53 and 0.11 m.s^{-1} for dissolution lengths of 50 and 100 μm respectively (Figure 9b). The difference between rates estimated with instantaneous and constant-rate assumptions primarily reflects the dependence of clinopyroxene dissolution rate on pressure (Figure 7). That is, clinopyroxene dissolution rates are much lower at depth where disequilibrium is negligible than at the surface where disequilibrium is greatest, meaning that very little clinopyroxene dissolves during the initial stages of clinopyroxene-undersaturated magma decompression.

Magma decompression rates estimated from clinopyroxene dissolution are compared with those estimated from the diffusive re-equilibration of primitive olivine crystals carried by the Borgarhraun magma in Figure 9c (Mutch et al., 2019b). Encouragingly, our best estimates (3.0–15 kPa.s^{-1}) are broadly comparable with those obtained from a wholly independent diffusion chronometry approach for the same eruption (0.7–3.3 kPa.s^{-1}). Our findings thus corroborate those of Mutch et al. (2019b) who estimated a mean magma ascent rate of 0.02–0.1 m.s^{-1}, and confirm that transcrustal magma transport in Iceland may be considerably more rapid than reported in arc settings (0.5–1 mm.s^{-1}; Ruprecht and Plank, 2013). On the basis of comparisons with transcrustal transport estimates from Mutch et al. (2019b), our best estimates also suggest that the Borgarhraun magma ascended more rapidly near the surface than it did at depth, consistent with either the upward acceleration of rising magma or the convolution of isobaric intervals of magma mixing with polybaric intervals of magma ascent by diffusion-based methods.

Magma decompression rates estimated for the Borgarhraun eruption are compared with published estimates from other basaltic systems in Figure 9c. Note that we compare decompression rather than ascent rates in order to avoid introducing additional uncertainties from converting pressures to depths across a range of different settings with different crustal density structures. Perhaps unsurprisingly, our best decompression rate estimates for the Borgarhraun eruption (3.0–15 kPa.s^{-1}) are about two orders of magnitude lower than those reported for the sub-plinian 1974 eruption of Volcán de Fuego, Guatemala, based on the loss of volatiles from melt embayments and the loss of H_2O from olivine crystals (240–600 and 380–450 kPa.s^{-1} respectively; Lloyd et al., 2014; Newcombe et al., 2020). Decompression rates estimated from the loss of volatiles from melt embayments for a series of hawaiian to sub-plinian eruptions of Kīlauea, Hawaii, are also greater than those estimated for the Borgarhraun eruption (50–450 kPa.s^{-1}), with the greatest Kīlauean rates being associated with the most explosive, sub-plinian eruptions (Ferguson et al., 2016). Indeed, decompression rates estimated for episode 1 of the hawaiian 1959 Kīlauea Iki eruption from both the loss of volatiles from melt embayments and the loss of H_2O from olivine crystals are only about one order of magnitude greater than our estimates for the Borgarhraun eruption (∼50 kPa.s^{-1}; Ferguson et al., 2016; Newcombe et al., 2020). A similar one-magnitude offset with respect to the Borgarhraun eruption has also been estimated for the hawaiian 1977 eruption of Seguam, Alaska, using the same techniques (20–130 kPa.s^{-1} from embayments and 40–230 kPa.s^{-1} from olivine; Newcombe et al., 2020). Thus, magmas that have fed explosive basaltic eruptions ranging from hawaiian to sub-plinian in style have decompressed more rapidly than the magma that fed the Borgarhraun eruption. However, this does not appear to have been the case for all explosively erupted basaltic magmas.

Decompression rates estimated for two moderately explosive eruptions of Cerro Negro, Nicaragua, in 1992 (VEI3, likely vulcanian) and 1995 (VEI2, likely hawaiian) are broadly similar to those estimated for the Borgarhraun eruption, especially in the case of less explosive 1995 eruption (Barth et al., 2019; Newcombe et al., 2020). Specifically, rates estimated for the 1992 and 1995 eruptions from the loss of volatiles from melt embayments are 2.3–20 and 0.039–10 kPa.s^{-1} respectively (Barth et al., 2019), and

those from the loss of H_2O from olivine crystals are 7–12 and 3 kPa.s^{-1} respectively (Newcombe et al., 2020). Decompression rates comparable to those from the Borgarhraun eruption have also been reported for the vulcanian 2013 eruption of Chaparrastique, El Salvador, based on plagioclase dissolution textures ($\sim$3 kPa.s^{-1}; Scarlato et al., 2017). Although deep magma decompression rates of $\sim$16 and $\sim$2.2 Pa.s^{-1} beneath Mount Etna and Campi Flegrei, Italy, estimated from clinopyroxene textures by Armienti et al. (2013) and Bonechi et al. (2020) respectively are about three orders of magnitude lower than our best estimates for the Borgarhraun eruption, shallow decompression rates estimated for hawaiian eruptions of Mount Etna in 2011 on the basis of clinopyroxene-ilmenite re-equilibration are very similar to those we report here (1.3–13 kPa.s^{-1}; Mollo et al., 2015). Finally, we note that our estimated decompression rates overlap with those obtained by modelling the diffusive loss of H_2O from moderately evolved olivine-hosted melt inclusions in magmatic tephra collected during weakly hawaiian phases of the 2014–2015 Holuhraun eruption, Iceland (3–8 kPa.s^{-1}; Hartley et al., 2018). During its final ascent, the Borgarhraun magma therefore appears to have decompressed as rapidly as magmas that have fed various explosive basaltic eruptions ranging from hawaiian to vulcanian in style.

The magma decompression rates that both we and Mutch et al. (2019b) estimate for the dominantly effusive and at most transiently explosive Borgarhraun eruption are broadly consistent with recently established relationships between explosivity and magma decompression rate (e.g., Barth et al., 2019). Namely, we find that the effusively erupted Borgarhraun magma decompressed more slowly than the magmas that fed basaltic sub-plinian eruptions at Fuego and Kīlauea. However, differences in magma decompression rate are modest or even absent when comparing the Borgarhraun eruption with hawaiian and vulcanian eruptions at Cerro Negro, Chaparrastique and Mount Etna. Our calculations thus suggest that effusively erupted H_2O-poor basalts from ocean island and mid-ocean ridge settings can decompress and ascend through the shallow crust just as rapidly as some explosively erupted H_2O-rich basalts from arc settings. Moreover, it seems unlikely that the ascent rates of basaltic magmas are simply related to their H_2O contents. Although H_2O exsolution certainly plays a major role in driving the ascent of myriad magma types, other factors such as melt buoyancy and CO_2 exsolution must therefore drive the rapid ascent of primitive and H_2O basalts like the Borgarhraun magma.

Comparing rates of shallow, syn-eruptive magma decompression (including our estimate for the Borgarhraun eruption) with those for deep decompression associated with inter-eruptive magma assembly beneath Mount Etna and Campi Flegrei (Figure 9c; Armienti et al., 2013; Bonechi et al., 2020), suggests that magmas ascend much more rapidly during eruptions than during pre-eruptive magma recharge events at depth. Magma transport leading to eruption may therefore operate in a fundamentally different way from magma transport out of the mantle and between magma reservoirs. It thus remains unclear how well seismic signals of inter-eruptive magma transport reflect likely rates of pre-eruptive magma ascent (White et al., 2011; Tarasewicz et al., 2012; Mutch et al., 2019b). Indeed, our results suggest that primitive and H_2O-poor basalts may erupt with no more than a few days' precursory warning, making it challenging to evaluate the risks posed by some basaltic volcanoes.

7 CONCLUSIONS

Mineral textures and compositions in a wehrlitic nodule from the primitive Borgarhraun lava flow erupted in North Iceland record clinopyroxene dissolution during magma ascent from near-Moho depths. Mapping the distribution of Al distinguishes high-Al_2O_3 clinopyroxene cores from low-Al_2O_3 clinopyroxene rims and inclusions. The high Al_2O_3 content of clinopyroxene cores is consistent with crystallisation at $\sim$800 MPa, in line with published estimates of pre-eruptive magma storage pressures. In contrast,

the low Al_2O_3 of clinopyroxene rims and inclusions is consistent with crystallisation at or near the surface. Given that clinopyroxene rim and inclusion boundaries cut across sector zone boundaries within resorbed clinopyroxene cores, we infer that high-Al_2O_3 clinopyroxene cores dissolved during ascent as a consequence of the strong dependence of clinopyroxene stability on pressure. We thus interpret clinopyroxene rims and inclusions as recrystallised boundary layers protected from convective or turbulent dissipation by their host nodule. Corroborating evidence for clinopyroxene dissolution is provided by plagioclase and titanomagnetite crystals within clinopyroxene rims and inclusions that occur in proportions consistent with low-pressure crystallisation of molten high-Al_2O_3 clinopyroxene cores during lava flow emplacement. Our findings are supported by textural and geochemical observations from across Iceland that indicate a potentially widespread role for clinopyroxene dissolution in basalt petrogenesis. It thus seems feasible that clinopyroxene dissolution could occur within any vertically extensive basaltic plumbing system and could hence offer a compelling explanation for the pyroxene paradox reported from mid-ocean ridge basalts.

Experimental calibrations of clinopyroxene stability suggest clinopyroxene began to dissolve once the Borgarhraun magma decompressed below the pressure of clinopyroxene saturation at 215 MPa. Our best decompression rate estimates of 3.0–15 kPa.s^{-1} were obtained from calculations assuming that decompression took place at a constant rate. These estimates could nonetheless be improved in future by quantifying the effects of mineral anisotropy on clinopyroxene dissolution kinetics with further experiments. Converting magma decompression rates into magma ascent rates results in values of 0.11–0.53 m.s^{-1} that are similar published estimates obtained from the diffusive re-equilibration of olivine (Mutch et al., 2019b). Nevertheless, our ascent rates are slightly higher than these published values, consistent with magma acceleration during ascent or the temporary stalling of magma after mush disaggregation. Although the Borgarhraun eruption broadly conforms to global correlations between eruption explosivities and magma decompression rates, the decompression rates we estimate are comparable to those obtained from some moderately explosive basaltic eruptions in arc settings, implying that there is no simple relationship between magma decompression rate and magma H_2O content. Indeed, comparing magma ascent rates from Iceland with those from arc settings suggests that primitive and H_2O-poor basalts can traverse the crust considerably faster than some H_2O-rich basalts, though further work is required to evaluate how ascent rates are affected by the differing structures of mid-ocean ridge, ocean island and arc plumbing systems. It is however clear that magmas tapped from reservoirs near the Moho in ocean island and mid-ocean ridge settings may reach the surface within days. This represents a major challenges when evaluating the risks posed by infrequent but nonetheless potentially hazardous eruptions of primitive basalt.

AUTHOR CONTRIBUTIONS

DAN and JM co-designed the project. DAN performed BSE imaging and EPMA, implemented the clinopyroxene dissolution model and wrote the manuscript. JM collected the sample, facilitated QEMSCAN imaging, rearranged the equations of Chen and Zhang (2009) and contributed to writing the manuscript.

FUNDING

DAN and this work were supported by a Presidential Fellowship from the University of Manchester.

ACKNOWLEDGEMENTS

We thank Lewis Hughes for assisting with BSE imaging at the University of Manchester and Iris Buisman for performing QEMSCAN imaging and assisting with EPMA at the University of Cambridge. We also thank Chiara Maria Petrone and Silvio Mollo for their insightful and constructive reviews, and Mattia Pistone for his efficient editorial handling.

SUPPLEMENTAL DATA

QEMSCAN images and EPMA data are provided in supplementary files.

REFERENCES

Aoki, K. and Kushiro, I. (1968). Some clinopyroxenes from ultramafic inclusions in Dreiser Weiher, Eifel. *Contributions to Mineralogy and Petrology* 18, 326–337. doi:10.1007/BF00399694

Armienti, P., Perinelli, C., and Putirka, K. D. (2013). A new model to estimate deep-level magma ascent rates, with applications to Mt. Etna (Sicily, Italy). *Journal of Petrology* 54, 795–813. doi:10.1093/petrology/egs085

Barth, A., Newcombe, M., Plank, T., Gonnermann, H., Hajimirza, S., Soto, G. J., et al. (2019). Magma decompression rate correlates with explosivity at basaltic volcanoes — Constraints from water diffusion in olivine. *Journal of Volcanology and Geothermal Research* 387, 106664. doi:10.1016/j.jvolgeores.2019.106664

Bender, J. F., Hodges, F. N., and Bence, A. E. (1978). Petrogenesis of basalts from the project FAMOUS area: experimental study from 0 to 15 kbars. *Earth and Planetary Science Letters* 41, 277–302. doi:10.1016/0012-821X(78)90184-X

Blundy, J. D., Falloon, T. J., Wood, B. J., and Dalton, J. A. (1995). Sodium partitioning between clinopyroxene and silicate melts. *Journal of Geophysical Research: Solid Earth* 100, 15501–15515

Bonechi, B., Perinelli, C., and Gaeta, M. (2020). Clinopyroxene growth rates at high pressure: constraints on magma recharge of the deep reservoir of the Campi Flegrei Volcanic District (south Italy). *Bulletin of Volcanology* 82. doi:10.1007/s00445-019-1342-5

Brearley, M. and Scarfe, C. M. (1986). Dissolution rates of upper mantle minerals in an alkali basalt melt at high pressure: An experimental study and implications for ultramafic xenolith survival. *Journal of Petrology* 27, 1157–1182. doi:10.1093/petrology/27.5.1157

Cashman, K. V., Sparks, R. S. J., and Blundy, J. D. (2017). Vertically extensive and unstable magmatic systems: A unified view of igneous processes. *Science* 355, eaag3055. doi:10.1126/science.aag3055

Cassidy, M., Manga, M., Cashman, K. V., and Bachmann, O. (2018). Controls on explosive-effusive volcanic eruption styles. *Nature Communications* 9, 2839. doi:10.1038/s41467-018-05293-3

Chen, Y. and Zhang, Y. (2008). Olivine dissolution in basaltic melt. *Geochimica et Cosmochimica Acta* 72, 4756–4777. doi:10.1016/j.gca.2009.06.016

Chen, Y. and Zhang, Y. (2009). Clinopyroxene dissolution in basaltic melt. *Geochimica et Cosmochimica Acta* 73, 5730–5747. doi:10.1016/j.gca.2009.06.016

Cooper, G. F., Davidson, J. P., and Blundy, J. D. (2016). Plutonic xenoliths from Martinique, Lesser Antilles: evidence for open system processes and reactive melt flow in island arc crust. *Contributions to Mineralogy and Petrology* 171, 87. doi:10.1007/s00410-016-1299-8

Crank, J. (1975). *The Mathematics of Diffusion* (Oxford: Clarendon Press), 2 edn.

Dohmen, R. and Milke, R. (2010). Diffusion in Polycrystalline Materials: Grain Boundaries, Mathematical Models, and Experimental Data. *Reviews in Mineralogy and Geochemistry* 72, 921–970

Eason, D. E. and Sinton, J. M. (2009). Lava shields and fissure eruptions of the Western Volcanic Zone, Iceland: Evidence for magma chambers and crustal interaction. *Journal of Volcanology and Geothermal Research* 186, 331–348. doi:10.1016/j.jvolgeores.2009.06.009

Ferguson, D. J., Gonnermann, H. M., Ruprecht, P., Plank, T. A., Hauri, E. H., Houghton, B. F., et al. (2016). Magma decompression rates during explosive eruptions of Kīlauea volcano, Hawaii, recorded by melt embayments. *Bulletin of Volcanology* 78, 71. doi:10.1007/s00445-016-1064-x

Freer, R., Carpenter, M. A., Long, J. V. P., and Reed, S. J. B. (1982). "Null result" diffusion experiments with diopside: implications for pyroxene equilibria. *Earth and Planetary Science Letters* 58, 285–292

Fujii, T. and Bougault, H. (1983). Melting relations of a magnesian abyssal tholeiite and the origin of MORBs. *Earth and Planetary Science Letters* 62, 283–295. doi:10.1016/0012-821X(83)90091-2

Ghiorso, M. S. and Sack, R. O. (1995). Chemical mass transfer in magmatic processes IV. A revised and internally consistent thermodynamic model for the interpolation and extrapolation of liquid-solid equilibria in magmatic systems at elevated temperatures and pressures. *Contributions to Mineralogy and Petrology* 119, 197–212. doi:10.1007/BF00307281

Gonnermann, H. M. and Manga, M. (2007). The Fluid Mechanics Inside a Volcano. *Annual Review of Fluid Mechanics* 39, 321–356. doi:10.1146/annurev.fluid.39.050905.110207

Grove, T. L., Kinzler, R. J., and Bryan, W. B. (1992). Fractionation of Mid-Ocean Ridge Basalt (MORB). In *Mantle Flow and Melt Generation at Mid-Ocean Ridges, Geophysical Monograph 71* (Washington D.C.: American Geophysical Union). 281–310

Gurenko, A. A. and Sobolev, A. V. (2006). Crust-primitive magma interaction beneath neovolcanic rift zone of Iceland recorded in gabbro xenoliths from Midfell, SW Iceland. *Contributions to Mineralogy and Petrology* 151, 495–520. doi:10.1007/s00410-006-0079-2

Halldórsson, S. A., Óskarsson, N., Grönvold, K., Sigurdsson, G., Sverrisdottir, G., and Steinthórsson, S. (2008). Isotopic-heterogeneity of the Thjorsa lava-Implications for mantle sources and crustal processes within the Eastern Rift Zone, Iceland. *Chemical Geology* 255, 305–316. doi:10.1016/j.chemgeo.2008.06.050

Hansen, H. and Grönvold, K. (2000). Plagioclase ultraphyric basalts in Iceland: The mush of the rift. *Journal of Volcanology and Geothermal Research* 98, 1–32. doi:10.1016/S0377-0273(99)00189-4

Hansteen, T. H. (1991). Multi-stage evolution of the picritic Mælifell rocks, SW Iceland: constraints from mineralogy and inclusions of glass and fluid in olivine. *Contributions to Mineralogy and Petrology* 109, 225–239. doi:10.1007/BF00306481

Hartley, M. E., Bali, E., Maclennan, J., Neave, D. A., and Halldórsson, S. A. (2018). Melt inclusion constraints on petrogenesis of the 2014–2015 Holuhraun eruption, Iceland. *Contributions to Mineralogy and Petrology* 173, 10. doi:10.1007/s00410-017-1435-0

Holland, T. J. B., Green, E. C. R., and Powell, R. (2018). Melting of peridotites through to granites: a simple thermodynamic model in the system KNCFMASHTOCr. *Journal of Petrology* 59, 881–900. doi:10.1093/petrology/egy048

Holness, M. B., Anderson, A. T., Martin, V. M., Maclennan, J., Passmore, E., and Schwindinger, K. R. (2007). Textures in partially solidified crystalline nodules: A window into the pore structure of slowly cooled mafic intrusions. *Journal of Petrology* 48, 1243–1264. doi:10.1093/petrology/egm016

Holness, M. B., Stripp, G., Humphreys, M. C. S., Veksler, I. V., Nielsen, T. F. D., and Tegner, C. (2011). Silicate liquid immiscibility within the crystal mush: late-stage magmatic microstructures in the skaergaard intrusion, east greenland. *Journal of Petrology* 52, 175–222. doi:10.1093/petrology/egq077

Humphreys, M. C. S., Menand, T., Blundy, J. D., and Klimm, K. (2008). Magma ascent rates in explosive eruptions: Constraints from H2O diffusion in melt inclusions. *Earth and Planetary Science Letters* 270, 25–40. doi:10.1016/j.epsl.2008.02.041

Jarosewich, E., Gooley, R., and Husler, J. (1987). Chromium Augite - A New Microprobe Reference Sample. *Geostandards and Geoanalytical Research* 11, 197–198. doi:10.1111/j.1751-908X.1987.tb00027.x

Jarosewich, E., Nelen, J. A., and Norberg, J. A. (1980). Reference samples for electron microprobe analysis. *Geostandards Newsletter* 4, 43–47

Katz, R. F., Spiegelman, M., and Langmuir, C. H. (2003). A new parameterization of hydrous mantle melting. *Geochemistry, Geophysics, Geosystems* 4, 1–19. doi:10.1029/2002GC000433

Kerr, R. C. (1995). Convective crystal dissolution. *Contributions to Mineralogy and Petrology* 121, 237–246. doi:10.1007/BF02688239

La Spina, G., Burton, M., and de' Michieli Vitturi, M. (2015). Temperature evolution during magma ascent in basaltic effusive eruptions: A numerical application to Stromboli volcano. *Earth and Planetary Science Letters* 426, 89–100. doi:10.1016/j.epsl.2015.06.015

La Spina, G., Clarke, A. B., de' Michieli Vitturi, M., Burton, M., Allison, C. M., Roggensack, K., et al. (2019). Conduit dynamics of highly explosive basaltic eruptions: The 1085 CE Sunset Crater sub-Plinian events. *Journal of Volcanology and Geothermal Research* 387, 106658. doi:10.1016/j.jvolgeores.2019.08.001

Liang, Y., Richter, F. M., and Watson, E. B. (1996). Diffusion in silicate melts: II. Multicomponent diffusion in CaO–Al2O3–SiO2 at 1500 °C and 1 GPa. *Geochimica et Cosmochimica Acta* 60, 5021–5035. doi:10.1016/S0016-7037(96)00352-3

Lindsley, D. H. and Andersen, D. J. (1983). A two-pyroxene thermometer. *Journal of Geophysical Research* 88 Supplem, A887–A906. doi:10.1029/JB088iS02p0A887

Lloyd, A. S., Ruprecht, P., Hauri, E. H., Rose, W., Gonnermann, H. M., and Plank, T. A. (2014). NanoSIMS results from olivine-hosted melt embayments: Magma ascent rate during explosive basaltic eruptions. *Journal of Volcanology and Geothermal Research* 283, 1–18. doi:10.1016/j.jvolgeores.2014.06.002

Maclennan, J. (2008). Concurrent mixing and cooling of melts under Iceland. *Journal of Petrology* 49, 1931–1953. doi:10.1093/petrology/egn052

Maclennan, J. (2019). Mafic tiers and transient mushes: evidence from Iceland. *Philosophical Transactions of the Royal Society A* 377, 20180021. doi:10.1098/rsta.2018.0021

Maclennan, J., Gaetani, G. A., Hartley, M. E., Neave, D. A., and Winpenny, B. (2012). Petrological constraints on the crustal structure under rift zones. In *AGU Fall Meeting Abstracts*. T41G

Maclennan, J., McKenzie, D., Grönvold, K., Shimizu, N., Eiler, J. M., and Kitchen, N. (2003a). Melt mixing and crystallization under Theistareykir, northeast Iceland. *Geochemistry, Geophysics, Geosystems* 4, 1–40. doi:10.1029/2003GC000558

Maclennan, J., McKenzie, D., Grönvold, K., and Slater, L. (2001). Crustal accretion under Northern Iceland. *Earth and Planetary Science Letters* 191, 295–310. doi:10.1016/S0012-821X(01)00420-4

Maclennan, J., McKenzie, D., Hilton, F., Grönvold, K., and Shimizu, N. (2003b). Geochemical variability in a single flow from northern Iceland. *Journal of Geophysical Research* 108, 1–21. doi:10.1029/2000JB000142

Magee, C., Stevenson, C. T. E., Ebmeier, S. K., Keir, D., Hammond, J. O. S., Gottsmann, J. H., et al. (2018). Magma Plumbing Systems: A Geophysical Perspective. *Journal of Petrology* 59, 1217–1251. doi:10.1093/petrology/egy064

Marsh, B. D. (2004). A magmatic mush column Rosetta stone: The McMurdo Dry Valleys of Antarctica. *Eos, Transactions American Geophysical Union* 85, 497–508. doi:10.1029/2004EO470001

730 Mastin, L. G. (2002). Insights into volcanic conduit flow from an open-source numerical model.
731 *Geochemistry, Geophysics, Geosystems* 3, 1–18. doi:10.1029/2001GC000192
732 Michael, P. J. (1988). The concentration, behavior and storage of H2O in the suboceanic upper mantle:
733 Implications for mantle metasomatism. *Geochimica et Cosmochimica Acta* 52, 555–566. doi:10.1016/
734 0016-7037(88)90110-X
735 Miller, W. G. R., Maclennan, J., Shorttle, O., Gaetani, G. A., Le Roux, V., and Klein, F. (2019). Estimating
736 the carbon content of the deep mantle with Icelandic melt inclusions. *Earth and Planetary Science*
737 *Letters* 523, 115699. doi:10.1016/j.epsl.2019.07.002
738 Mollo, S., Del Gaudio, P., Ventura, G., Iezzi, G., and Scarlato, P. (2010). Dependence of clinopyroxene
739 composition on cooling rate in basaltic magmas: Implications for thermobarometry. *Lithos* 118, 302–312.
740 doi:10.1016/j.lithos.2010.05.006
741 Mollo, S., Giacomoni, P. P., Andronico, D., and Scarlato, P. (2015). Clinopyroxene and titanomagnetite
742 cation redistributions at Mt. Etna volcano (Sicily, Italy): Footprints of the final solidification history of
743 lava fountains and lava flows. *Chemical Geology* 406, 45–54. doi:10.1016/j.chemgeo.2015.04.017
744 Mutch, E. J. F., Maclennan, J., Holland, T. J. B., and Buisman, I. (2019a). Millennial storage of near-Moho
745 magma. *Science* 264, 260–264. doi:10.1126/science.aax4092
746 Mutch, E. J. F., Maclennan, J., Shorttle, O., Edmonds, M., and Rudge, J. F. (2019b). Rapid transcrustal
747 magma movement under Iceland. *Nature Geoscience* 12, 569–574. doi:10.1038/s41561-019-0376-9
748 Namiki, A. and Manga, M. (2006). Influence of decompression rate on the expansion velocity and
749 expansion style of bubbly fluids. *Journal of Geophysical Research: Solid Earth* 111, 1–17. doi:10.1029/
750 2005JB004132
751 Namiki, A. and Manga, M. (2008). Transition between fragmentation and permeable outgassing of
752 low viscosity magmas. *Journal of Volcanology and Geothermal Research* 169, 48–60. doi:10.1016/j.
753 jvolgeores.2007.07.020
754 Neave, D. A., Bali, E., Guðfinnsson, G. H., Halldórsson, S. A., Kahl, M., Schmidt, A.-S., et al. (2019a).
755 Clinopyroxene–liquid equilibria and geothermobarometry in natural and experimental tholeiites: the
756 2014–2015 Holuhraun eruption, Iceland. *Journal of Petrology* 60, 1653–1680. doi:10.1093/petrology/
757 egz042
758 Neave, D. A., Buisman, I., and Maclennan, J. (2017a). Continuous mush disaggregation during the
759 long-lasting Laki fissure eruption, Iceland. *American Mineralogist* 102, 2007–2021
760 Neave, D. A., Hartley, M. E., Maclennan, J., Edmonds, M., and Thordarson, T. (2017b). Volatile and light
761 lithophile elements in high-anorthite plagioclase-hosted melt inclusions from Iceland. *Geochimica et*
762 *Cosmochimica Acta* 205, 100–118. doi:10.1016/j.gca.2017.02.009
763 Neave, D. A., Maclennan, J., Hartley, M. E., Edmonds, M., and Thordarson, T. (2014). Crystal storage
764 and transfer in basaltic systems: the Skuggafjöll eruption, Iceland. *Journal of Petrology* 55, 2311–2346.
765 doi:10.1093/petrology/egu058
766 Neave, D. A., Namur, O., Shorttle, O., and Holtz, F. (2019b). Magmatic evolution biases basaltic records
767 of mantle chemistry towards melts from recycled sources. *Earth and Planetary Science Letters* 520,
768 199–211. doi:10.1016/j.epsl.2019.06.003
769 Neave, D. A. and Putirka, K. D. (2017). A new clinopyroxene-liquid barometer, and implications for
770 magma storage pressures under Icelandic rift zones. *American Mineralogist* 102, 777–794. doi:10.2138/
771 am-2017-5968
772 Newcombe, M. E., Plank, T., Barth, A., Asimow, P., and Hauri, E. (2020). Water-in-olivine magma
773 ascent chronometry: Every crystal is a clock. *Journal of Volcanology and Geothermal Research*
774 doi:10.1016/j.jvolgeores.2020.106872

O'Donnell, T. and Presnall, D. C. (1980). Chemical variations of the glass and mineral phases in basalts dredged from 25–30 N along the Mid-Atlantic Ridge. *American Journal of Science* 280, 845–868

Pearson, D. G., Canil, D., and Shirey, S. B. (2003). Mantle Samples Included in Volcanic Rocks: Xenoliths and Diamonds. *Treatise on Geochemistry* 2-9, 171–275. doi:10.1016/B0-08-043751-6/02005-3

Peslier, A. H., Bizimis, M., and Matney, M. (2015). Water disequilibrium in olivines from Hawaiian peridotites: Recent metasomatism, H diffusion and magma ascent rates. *Geochimica et Cosmochimica Acta* 154, 98–117. doi:10.1016/j.gca.2015.01.030

Pirrie, D., Butcher, A. R., Power, M. R., Gottlieb, P., and Miller, G. L. (2004). Rapid quantitative mineral and phase analysis using automated scanning electron microscopy (QemSCAN); potential applications in forensic geoscience. *Geological Society, London, Special Publications* 232, 123–136. doi:10.1144/GSL.SP.2004.232.01.12

Presnall, D. C., Dixon, S. A., Dixon, J. R., O'Donnell, T. H., Brenner, N. L., Schrock, R. L., et al. (1978). Liquidus Phase Relations on the Join Diopside-Forsterite-Anorthite from 1 atm to 20 kbar: Their Bearing on the Generation and Crystallization of Basaltic Magma. *Contributions to Mineralogy and Petrology* 66, 203–220. doi:10.1007/BF00372159

Putirka, K. D. (2008). Thermometers and Barometers for Volcanic Systems. *Reviews in Mineralogy and Geochemistry* 69, 61–120. doi:10.2138/rmg.2008.69.3

Putirka, K. D., Johnson, M., Kinzler, R. J., Longhi, J., and Walker, D. (1996). Thermobarometry of mafic igneous rocks based on clinopyroxene-liquid equilibria, 0–30 kbar. *Contributions to Mineralogy and Petrology* 123, 92–108. doi:10.1007/s004100050145

R Development Core Team (2016). R: A Language and Environment for Statistical Computing. *R Foundation for Statistical Computing*

Rudnick, R. L. (1992). Xenoliths - Samples of the lower continental crust. *Continental Lower Crust* 23, 269–316

Ruprecht, P. and Plank, T. A. (2013). Feeding andesitic eruptions with a high-speed connection from the mantle. *Nature* 500, 68–72. doi:10.1038/nature12342

Rutherford, M. J. (2008). Magma Ascent Rates. *Reviews in Mineralogy and Geochemistry* 69, 241–271. doi:10.2138/rmg.2008.69.7

Saal, A. E., Hauri, E. H., Langmuir, C. H., and Perfit, M. R. (2002). Vapour undersaturation in primitive mid-ocean-ridge basalt and the volatile content of Earth's upper mantle. *Nature* 419, 451–455. doi:10.1038/nature01073

Scarlato, P., Mollo, S., Del Bello, E., von Quadt, A., Brown, R. J., Gutierrez, E., et al. (2017). The 2013 eruption of Chaparrastique volcano (El Salvador): Effects of magma storage, mixing, and decompression. *Chemical Geology* 448, 110–122. doi:10.1016/j.chemgeo.2016.11.015

Shea, T., Lynn, K. J., and Garcia, M. O. (2015). Cracking the olivine zoning code: Distinguishing between crystal growth and diffusion. *Geology* 43, 935–938. doi:10.1130/G37082.1

Sigurdsson, I. A., Steinthórsson, S., and Grönvold, K. (2000). Calcium-rich melt inclusions in Cr-spinels from Borgarhraun, northern Iceland. *Earth and Planetary Science Letters* 183, 15–26. doi:10.1016/S0012-821X(00)00269-7

Smith, P. M. and Asimow, P. D. (2005). Adiabat-1ph: A new public front-end to the MELTS, pMELTS, and pHMELTS models. *Geochemistry, Geophysics, Geosystems* 6, 1–8. doi:10.1029/2004GC000816

Sparks, R. S. J., Annen, C., Blundy, J. D., Cashman, K. V., Rust, A. C., and Jackson, M. D. (2019). Formation and dynamics of magma reservoirs. *Philosophical Transactions of the Royal Society A* 377, 20180019. doi:10.1098/rsta.2018.0019

Sparks, R. S. J. and Cashman, K. V. (2017). Dynamic magma systems: implications for forecasting volcanic activity. *Elements* 13, 35–40. doi:10.2113/gselements.13.1.35

Staples, R. K., White, R. S., Brandsdóttir, B., Menke, W., Maguire, P. K. H., and McBride, J. H. (1997). Färoe-Iceland Ridge Experiment 1. Crustal structure of northeastern Iceland. *Journal of Geophysical Research: Solid Earth* 102, 7849–7866. doi:10.1029/96JB03911

Streck, M. J. (2008). Mineral Textures and Zoning as Evidence for Open System Processes. *Reviews in Mineralogy and Geochemistry* 69, 595–622. doi:10.2138/rmg.2008.69.15

Sugawara, T. (2000). Empirical relationships between temperature, pressure, and MgO content in olivine and pyroxene saturated liquid. *Journal of Geophysical Research* 105, 8457–8472. doi:10.1029/2000JB900010

Tarasewicz, J., Brandsdóttir, B., White, R. S., Hensch, M., and Thorbjarnardóttir, B. (2012). Using microearthquakes to track repeated magma intrusions beneath the Eyjafjallajkull stratovolcano, Iceland. *Journal of Geophysical Research: Solid Earth* 117, 1–13. doi:10.1029/2011JB008751

Thompson, G., Bryan, W. B., and Melson, W. G. (1980). Geological and Geophysical Investigation of the Mid-Cayman Rise Spreading Center: Geochemical Variation and Petrogenesis of Basalt Glasses Published by : The University of Chicago Press Stable URL : http://www.jstor.org/stable/30068479 Accessed : 21-03-2. *The Journal of Geology* 88, 41–55

Thompson, R. N. (1974). Some high-pressure pyroxenes. *Mineralogical Magazine* 39, 768–787. doi:10.1180/minmag.1974.039.307.04

Trønnes, R. G. (1990). Basaltic melt evolution of the Hengill volcanic system, SW Iceland, and evidence for clinopyroxene assimilation in primitive tholeiitic magmas. *Journal of Geophysical Research: Solid Earth* 95, 15893–15910. doi:10.1029/JB095iB10p15893

Tsuchiyama, A. (1986). Melting and dissolution kinetics: Application to partial melting and dissolution of xenoliths. *Journal of Geophysical Research* 91, 9395. doi:10.1029/JB091iB09p09395

Welsch, B., Hammer, J. E., Baronnet, A., Jacob, S., Hellebrand, E., and Sinton, J. M. (2016). Clinopyroxene in postshield Haleakala ankaramite 2. Texture, compositional zoning, and supersaturation in the magma. *Contributions to Mineralogy and Petrology* 171, 6. doi:10.1007/s00410-015-1213-9

White, R. S., Drew, J., Martens, H. R., Key, J., Soosalu, H., and Jakobsdóttir, S. S. (2011). Dynamics of dyke intrusion in the mid-crust of Iceland. *Earth and Planetary Science Letters* 304, 300–312. doi:10.1016/j.epsl.2011.02.038

Wilson, L. and Head, J. W. (1981). Ascent and eruption of basaltic magma on the earth and moon. *Journal of Geophysical Research: Solid Earth* 86, 2971–3001. doi:10.1029/JB086iB04p02971

Winpenny, B. and Maclennan, J. (2011). A partial record of mixing of mantle melts preserved in Icelandic phenocrysts. *Journal of Petrology* 52, 1791–1812. doi:10.1093/petrology/egr031

Woods, A. W. and Koyaguchi, T. (1994). Transitions between explosive and effusive eruptions of silicic magmas. *Nature* 370, 641–644. doi:10.1038/370641a0

Wright, H. M. N., Cashman, K. V., Mothes, P. A., Hall, M. L., Ruiz, A. G., and Le Pennec, J. L. (2012). Estimating rates of decompression from textures of erupted ash particles produced by 1999-2006 eruptions of Tungurahua volcano, Ecuador. *Geology* 40, 619–622. doi:10.1130/G32948.1

Yang, H.-J., Kinzler, R. J., and Grove, T. L. (1996). Experiments and models of anhydrous, basaltic olivine-plagioclase-augite saturated melts from 0.001 to 10 kbar. *Contributions to Mineralogy and Petrology* 124, 1–18. doi:10.1007/s004100050169

Yu, Y., Zhang, Y., Chen, Y., and Xu, Z. (2016). Kinetics of anorthite dissolution in basaltic melt. *Geochimica et Cosmochimica Acta* 179, 257–274. doi:10.1016/j.gca.2016.02.002

Zhang, X., Ganguly, J., and Ito, M. (2010a). Ca-Mg diffusion in diopside: Tracer and chemical inter-diffusion coefficients. *Contributions to Mineralogy and Petrology* 159, 175–186. doi:10.1007/s00410-009-0422-5

Zhang, Y., Ni, H., and Chen, Y. (2010b). Diffusion data in silicate melts. *Reviews in Mineralogy and Geochemistry* 72, 311–408. doi:10.2138/rmg.2010.72.8

Zhang, Y., Walker, D., and Lesher, C. E. (1989). Diffusive crystal dissolution. *Contributions to Mineralogy and Petrology* 102, 492–513. doi:10.1007/BF00371090

Zhang, Y. and Xu, Z. (2003). Kinetics of convective crystal dissolution and melting, with applications to methane hydrate dissolution and dissociation in seawater. *Earth and Planetary Science Letters* 213, 133–148. doi:10.1016/S0012-821X(03)00297-8

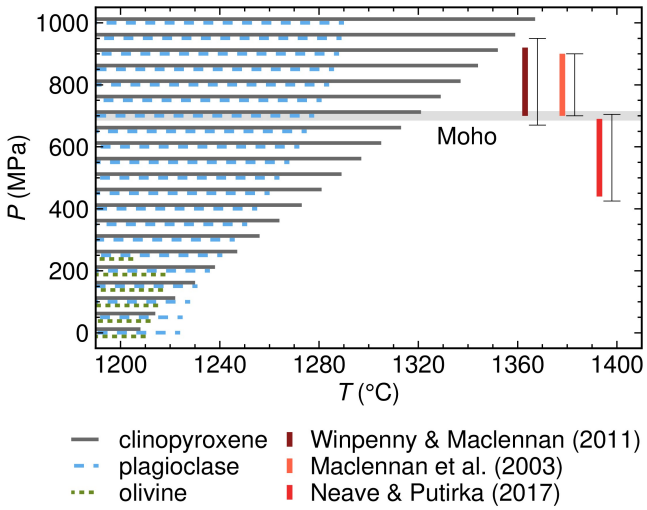

Figure 1. Mineral stabilities in the Borgarhraun lava flow from from North Iceland calculated with the MELTS algorithm (Ghiorso and Sack, 1995; Smith and Asimow, 2005). Calculations were performed using the matrix glass composition reported by Sigurdsson et al. (2000), and highlight the strong pressure dependence of clinopyroxene stability. Horizontal lines indicate the temperature ranges over which clinopyroxene, plagioclase and olivine are stable during isobaric fractional crystallisation at different pressures. The depth of the seismic Moho from Staples et al. (1997) is shown alongside petrological estimates of pre-eruptive magma storage pressures (Maclennan et al., 2003b; Winpenny and Maclennan, 2011; Neave and Putirka, 2017). Vertical coloured bars show 1σ uncertainties in pressure estimates; vertical error bars show model uncertainties expressed as standard errors of estimate (SEEs).

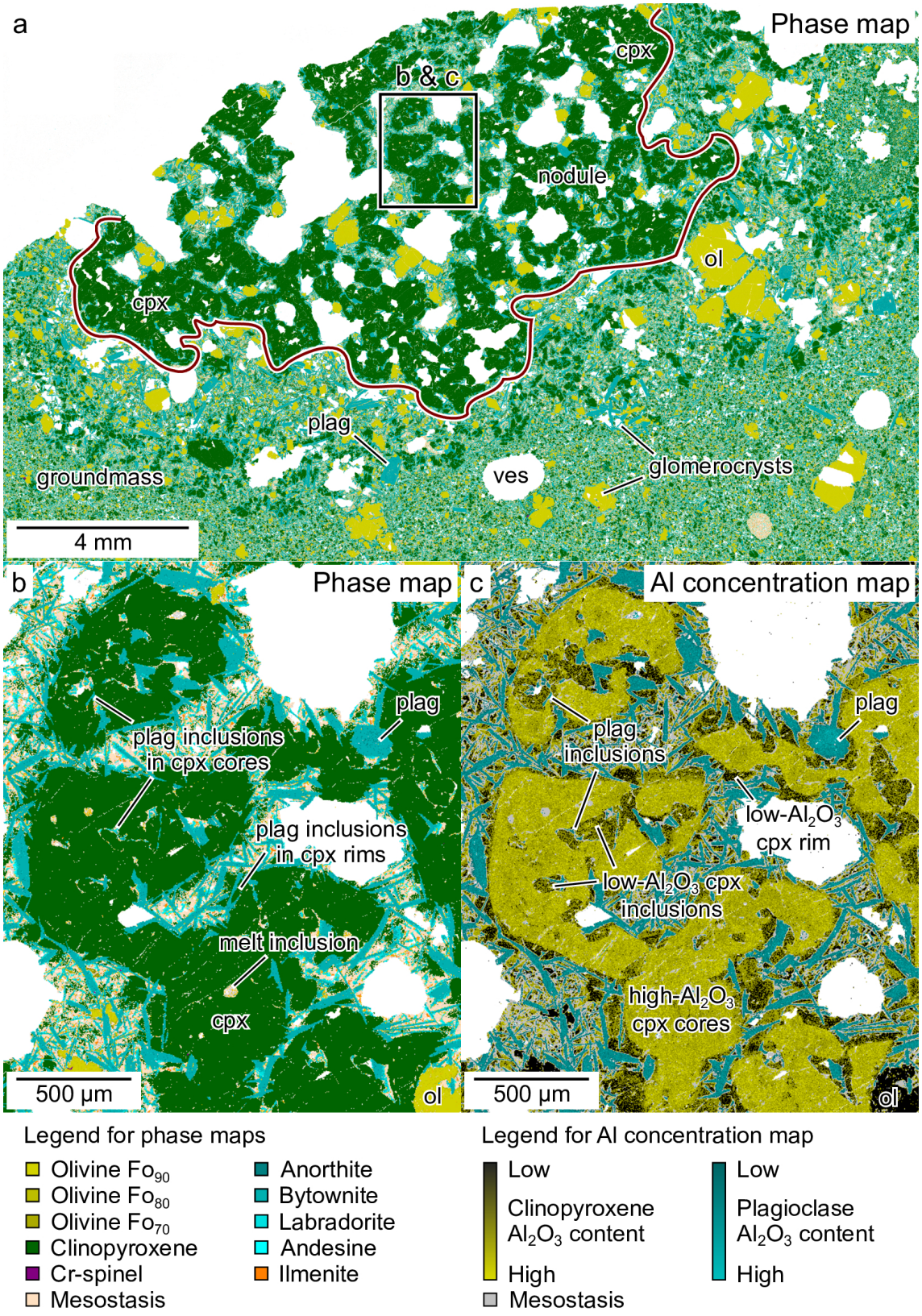

Figure 2. Phase and Al concentration maps of a wehrlitic nodule in sample JM27 from the Borgarhraun lava flow in North Iceland obtained by QEMSCAN. (a) The wehrlitic nodule is composed of clinopyroxne with subordinate olivine and rare plagioclase. It also contains pockets and channels of crystalline groundmass that are contiguous with the lava groundmass, indicating that the nodule was porous at the point of lava flow emplacement. Macrocrystic and glomerocrystic olivine, plagioclase and clinopyroxene also occur in the lava groundmass. (b) Plagioclase inclusions are present in the cores and rims of clinopyroxenes in the wehrlitic nodule. (c) Clinopyroxene cores in the wehrlitic nodule have relatively high Al_2O_3 contents, whereas clinopyroxene rims have relatively low Al_2O_3 contents. Plagioclase inclusions in clinopyroxene cores are associated with inclusions of low-Al_2O_3 clinopyroxene that are not evident in phase maps.

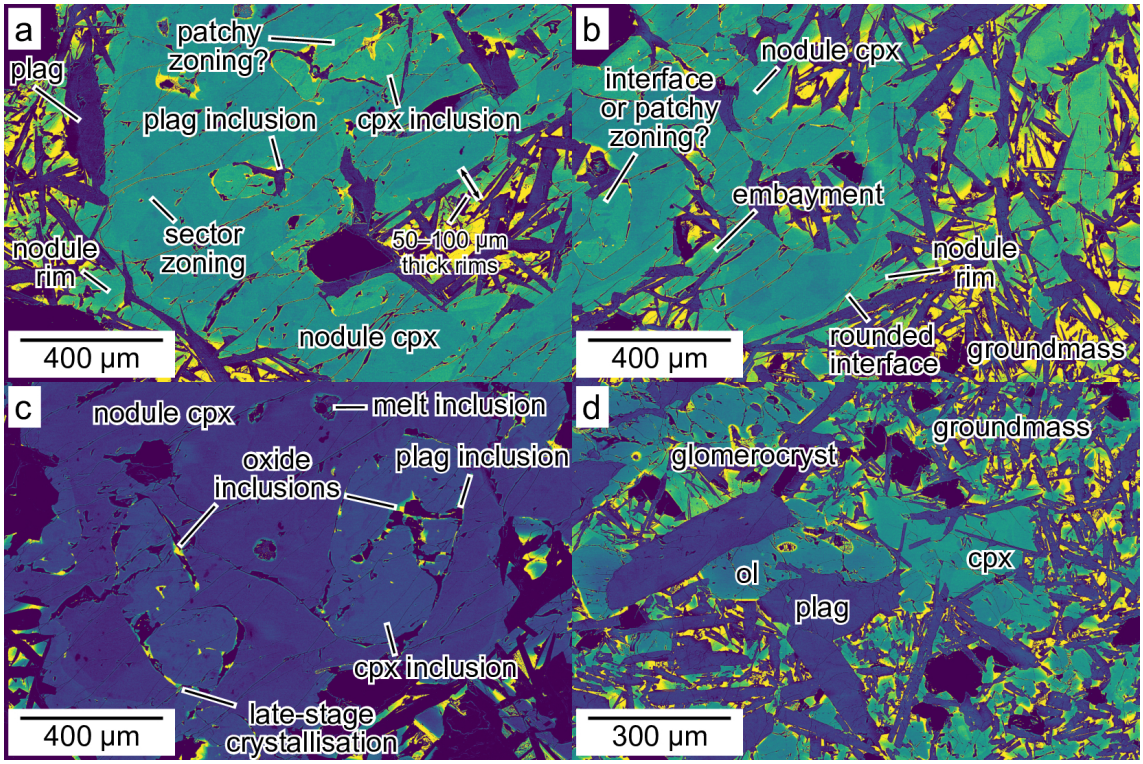

Figure 3. Backscattered electron (BSE) images of mineral textures in sample JM27 from the Borgarhraun lava flow in North Iceland. Raw and additional representative images are provided in the Supplementary Material. (a and b) Nodule clinopyroxene cores have low but variable BSE intensities consistent with the presence of sector zoning. Nodule clinopyroxene rims and inclusions have slightly higher BSE intensities that increase greatly towards the groundmass and pockets of late-stage crystallisation respectively. Nodule clinopyroxene rims and inclusions both contain irregular plagioclase inclusions. (c) Pockets of late-stage crystallisation within clinopyroxene inclusions have very high BSE intensities and are associated with both plagioclase and oxide (titanomagnetite) inclusions. (d) Macrocrystic and glomerocrystic olivine, plagioclase and clinopyroxene occur in the crystalline lava groundmass. Plagioclase macrocrysts and glomerocrysts are typically larger than plagioclase crystals in the wehrlitic nodule. Clinopyroxene macrocrysts and glomerocrysts are often arranged in ophitic arrangements with plagioclase.

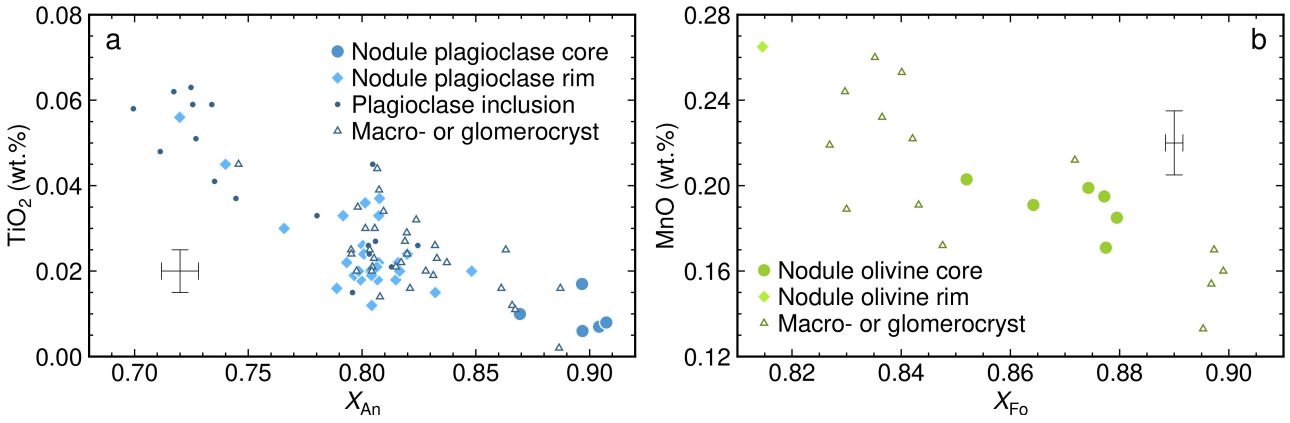

Figure 4. Plagioclase and olivine compositions in sample JM27 from the Borgarhraun lava flow in North Iceland. (a) Plagioclase compositions summarised in terms of X_{An} [where X_{An} = molar Ca/(Ca+Na)] and TiO_2. Analyses are divided into four textural associations: nodule cores, nodule rims, inclusions and macrocrysts or glomerocrysts. 2σ analytical uncertainties based on repeat measurements of the Lake County plagioclase (NMNH 115900) are shown (Jarosewich et al., 1980). (b) Olivine compositions summarised in terms of X_{Fo} [where X_{Fo} = molar Mg/(Mg+Fe)] and MnO. Analyses are divided into three textural associations: nodule cores, nodule rims and macrocrysts or glomerocrysts. 2σ analytical uncertainties based on repeat measurements of the San Carlos olivine (NMNH 111312-44) are shown (Jarosewich et al., 1980).

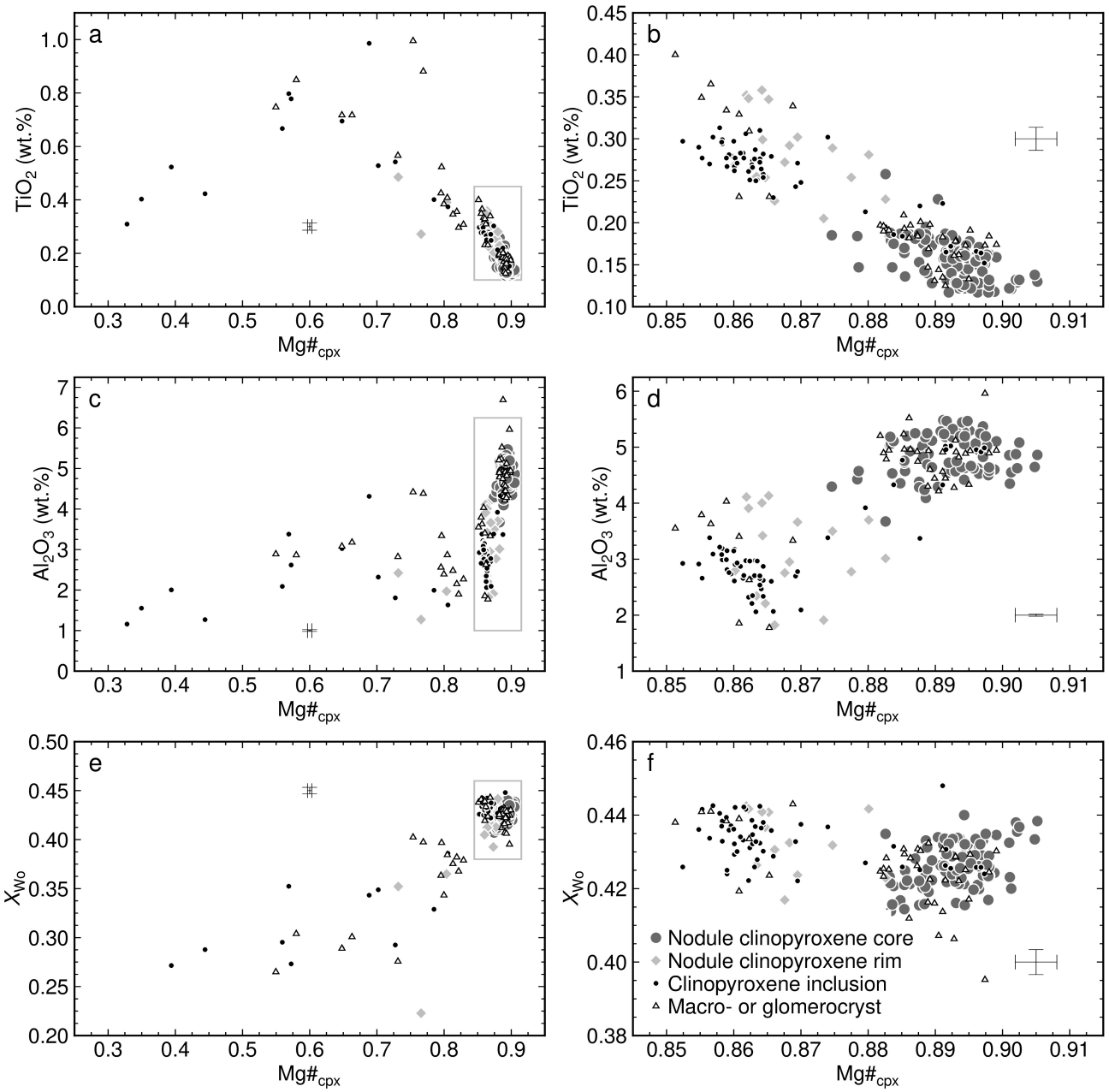

Figure 5. Clinopyroxene compositions in sample JM27 from the Borgarhraun lava flow in North Iceland. Analyses are divided into four textural associations: nodule cores, nodule rims, inclusions and macrocrysts or glomerocrysts. 2σ analytical uncertainties based on repeat measurements of the Ney County Cr-Augite (NMNH 164905) are shown (Jarosewich et al., 1987). (a and b) Plots of $Mg\#_{cpx}$ [where $Mg\#_{cpx}$ = molar Mg/(Mg+Fe)] versus TiO_2. (c and d) Plots of $Mg\#_{cpx}$ versus Al_2O_3. (e and f) Plots of $Mg\#_{cpx}$ versus wollastonite component [X_{Wo}, where X_{Wo} = Ca/(Ca+Mg+Fe) on a molar basis]. Panels (b, d and e) show the regions outlined with grey box in panels (a, c and e).

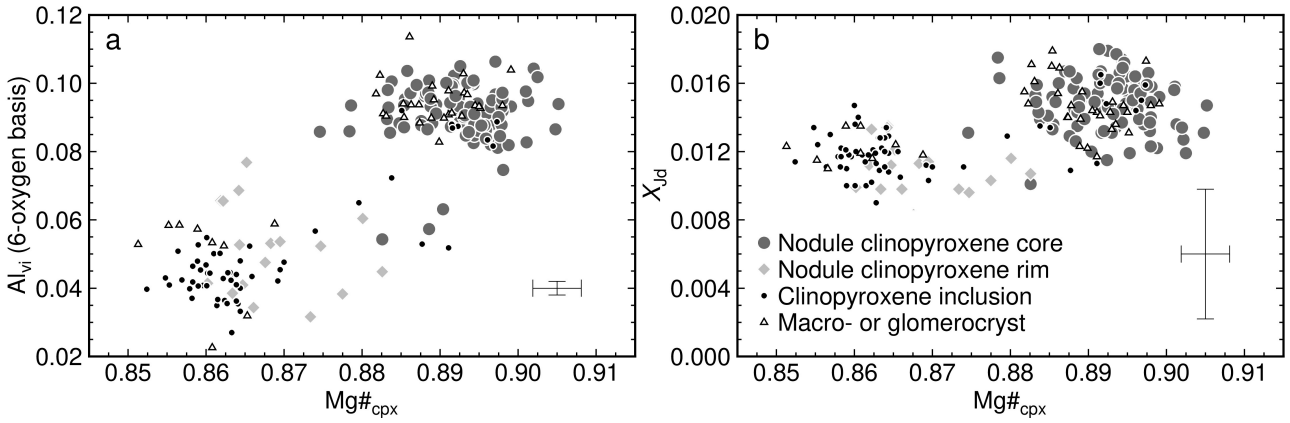

Figure 6. Variations in pressure-sensitive clinopyroxene components in sample JM27 from the Borgarhraun lava flow in North Iceland. Analyses are divided into four textural associations: nodule cores, nodule rims, inclusions and macrocrysts or glomerocrysts. 2σ analytical uncertainties based on repeat measurements of the Ney County Cr-Augite (NMNH 164905) are shown (Jarosewich et al., 1987). (a) Plot of Mg#$_{cpx}$ [where Mg#$_{cpx}$ = molar Mg/(Mg+Fe)] versus octahedral Al (Al_{vi}) calculated on a six-oxygen basis. (b) Plot of Mg#$_{cpx}$ versus jadeite component (X_{Jd}) content calculated following Putirka (2008).

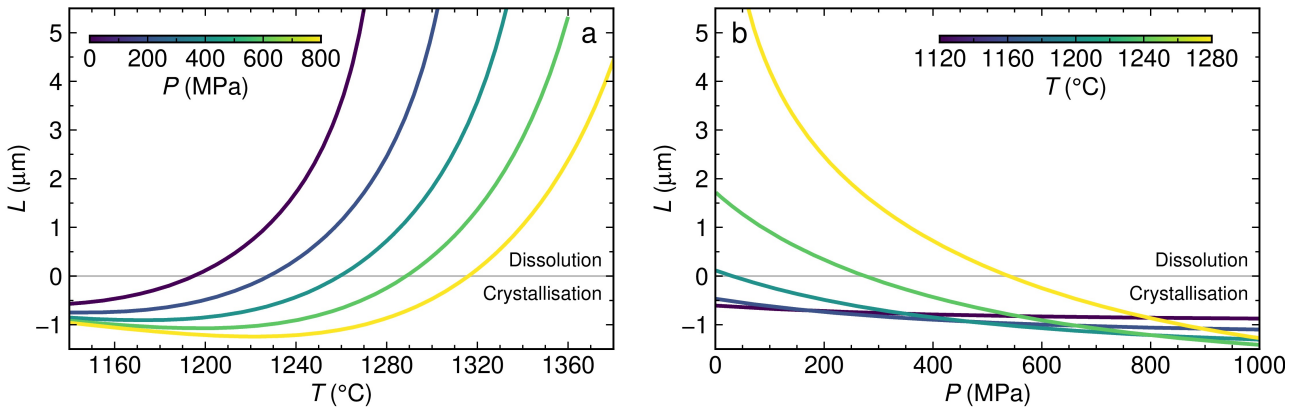

Figure 7. The stability of nodule clinopyroxene cores in the Borgarhraun lava flow as functions of pressure and temperature. Coloured lines show the length that the mean nodule clinopyroxene core composition is predicted to dissolve or crystallise in 1 s under different pressure and temperature conditions according to the model of Chen and Zhang (2009). Calculations were performed assuming dissolution into or crystallisation from the Borgarhraun matrix glass composition reported by Sigurdsson et al. (2000).

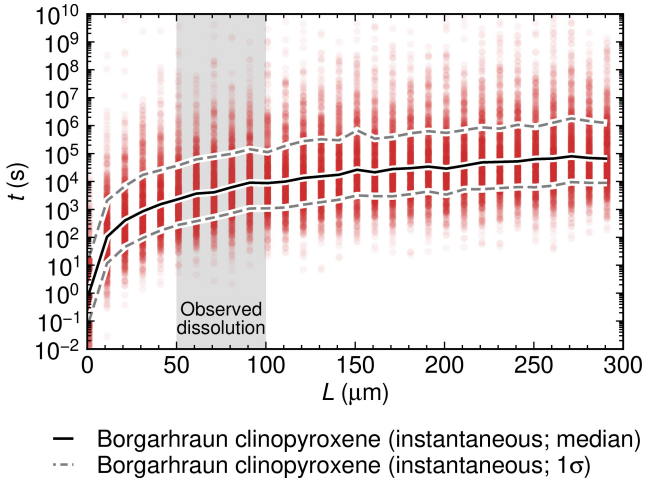

Figure 8. Dissolution time as a function of dissolution length for nodule clinopyroxene cores dissolving into the Borgarhraun matrix glass upon instantaneous ascent to the surface. Red points show the result of simulations performed to evaluate the effect of uncertainties in temperature and dissolution model fitting parameters (Sugawara, 2000; Mutch et al., 2019b; Chen and Zhang, 2009). The black line shows the median dissolution time at each dissolution length; dashed grey lines represent 1σ confidence intervals (i.e. 66% of simulations lie between the grey dashed lines). The vertical grey bar represents the range of clinopyroxene rim dissolution lengths identified from QEMSCAN and BSE images (Figures 2 and 3) that constrain our best estimates of minimum dissolution times.

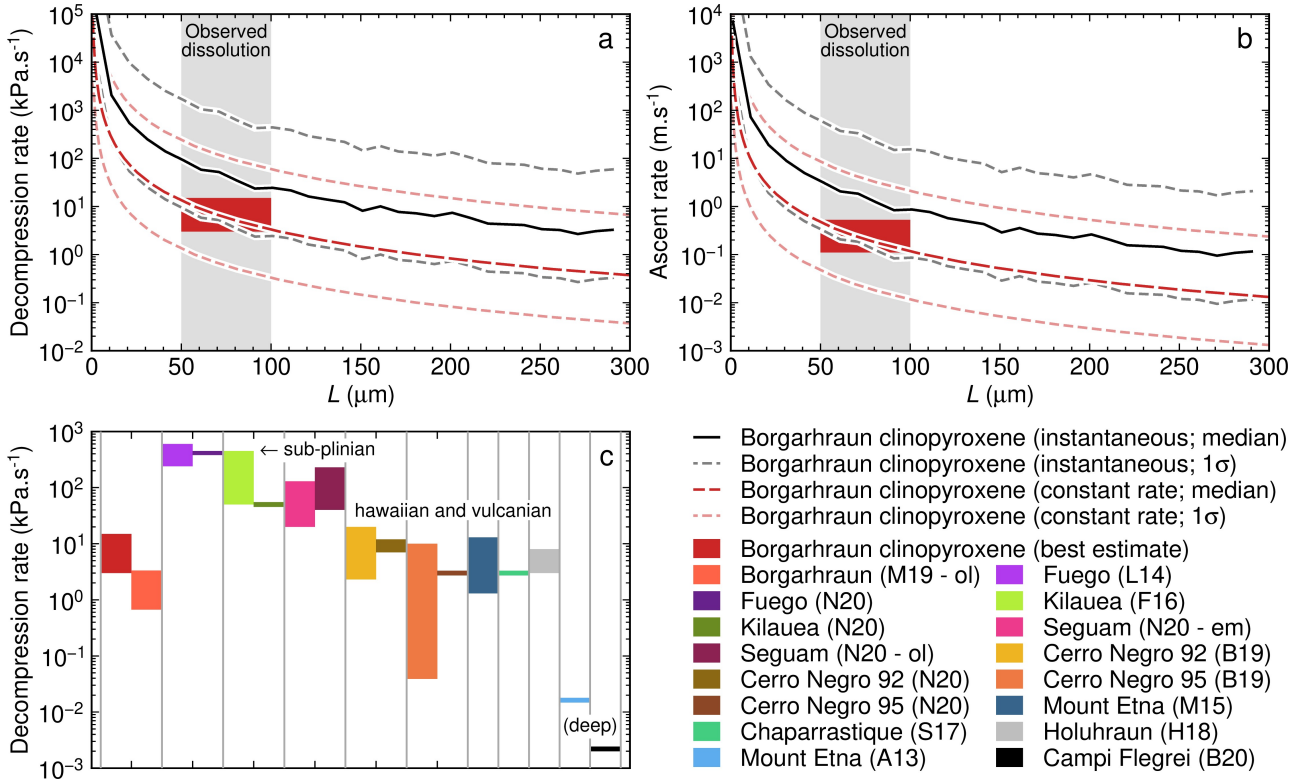

Figure 9. Magma decompression and ascent rates in basaltic systems. (a and b) Magma decompression and ascent rates are shown as functions of dissolution length for nodule clinopyroxene cores dissolving into the Borgarhraun matrix glass in panels (a) and (b) respectively. Solid black lines show decompression and ascent rates calculated using the dissolution times shown in Figure 8. These decompression and ascent rates represent mean values calculated with the simplifying assumption that all dissolution took place at the surface following instantaneous ascent. Dashed red lines show decompression and ascent rates calculated assuming that magma decompression and ascent took place at a constant rate from onset of clinopyroxene dissolution. The vertical grey bar represents the range of dissolution lengths identified from QEMSCAN and BSE images (Figures 2 and 3) that constrain our best estimates of magma decompression and ascent rates. (c) Literature estimates of magma decompression rate from basaltic systems compared with our best estimate for the Borgarhraun eruption. Methods and sources of decompression rate estimates are as follows: M19, olivine diffusion for the Borgarhraun eruption by Mutch et al. (2019b); L14, diffusive volatile loss from embayments for the 1974 eruption of Fuego by Lloyd et al. (2014); F16, diffusive volatile loss from embayments for various eruptions of Kīlauea by Ferguson et al. (2016); N20, diffusive volatile loss from embayments for the 1977 eruption of Seguam (em), and diffusive H_2O loss from olivine for episode 1 of the 1959 eruption of Kīlauea Iki, the 1974 eruption of Fuego, the 1992 and 1995 eruptions of Cerro Negro, and the 1977 eruption of Seguam (ol) by Newcombe et al. (2020); B19, diffusive volatile loss from olivine-hosted melt inclusions for the 1992 and 1995 eruptions of Cerro Negro by Barth et al. (2019); M15, clinopyroxene-ilmenite re-equilibration for the 2011 eruption of Mount Etna by Mollo et al. (2015); S17, plagioclase disequilibrium for the 2013 eruption of Chaparrastique by Scarlato et al. (2017); H18, diffusive volatile loss from olivine-hosted melt inclusions for the 2014–2015 Holuhraun eruption by Hartley et al. (2018); A13, clinopyroxene textures for deep magma ascent at Mount Etna by Armienti et al. (2013); and B20, clinopyroxene textures for deep magma ascent at Campi Flegrei by Bonechi et al. (2020).